Structures 70 (2024) 107848

Contents lists available at ScienceDirect

Structures

journal homepage: www.elsevier.com/locate/structures

A novel hysteretic restoring force model for shear link dampers: A machine learning approach

Ahmed Elgammal *, Yasmin Ali

Civil Engineering Department, College of Architecture and Environment, Sichuan University, Chengdu 610065, China

ARTICLE INFO

Keywords:
Cyclic loading
Hysteretic response
Material nonlinearity
Finite element
Genetic algorithm optimization
Artificial neural network

ABSTRACT

This research presents an enhanced restoring force model for shear link dampers along with a machine learning-based approach to predict its hardening parameters. The conducted work comprised three distinct phases. Initially, a numerical investigation utilizing ANSYS Workbench was conducted on 350 shear link dampers, taking into account the nonlinearity of the material as well as geometric imperfections. The study focused on the impact of geometric properties on key hysteretic parameters, and analytical formulas were derived to estimate shear yield strength, cyclic web shear buckling rotation angle, and elastic stiffness. In the second phase, the original restoring force model from earlier studies was enhanced and further simplified. Subsequently, a genetic algorithm implemented in MATLAB determined the optimal hardening parameters of the proposed model for each specimen, aligning the analytical hysteretic curves with those from the numerical study. Results indicated that the proposed model more accurately simulated shear link damper hysteretic response compared to the original model. The third and final phase involved constructing and training an artificial neural network (ANN) using hardening parameters obtained in the second phase as targets, with shear link damper geometric properties as inputs. The ANN demonstrated robust learning and high accuracy. To validate the efficiency of the proposed analytical model, blind testing against experimentally tested specimens was conducted, confirming that the model effectively mimicked the experimental hysteretic response of shear link dampers.

1. Introduction

Several advanced seismic-resistant systems have been proposed in the literature to protect structures during seismic events by modifying their dynamic behavior rather than the strength and stiffness of their main components [1]. Advanced systems are divided into four categories: passive, active, semi-active, and hybrid [2,3]. However, passive systems are considered the most reliable and dependable due to their low cost and ease of installation compared to other systems. Several families fall under the category of passive control systems, one of which is the yielding metallic damper family [4].

Among different types of yielding metallic dampers, shear (short) link dampers, shown in Fig. 1, have been widely tested due to their observed efficiency in dissipating seismic energy. They are carefully designed to first yield due to shear forces rather than bending moments, as this causes an increase in rotation and energy dissipation capacities [5]. This can be achieved by limiting the shear link damper length (e) as follows [6]:

$$e \leq 1.6M_P/V_P \tag{1}$$

where M_P and V_P are the plastic moment capacity and plastic shear capacity of the cross-section, respectively.

Popov et al. [5,7] indicated that properly dimensioning shear link dampers leads to ductile hysteretic behavior. The length ratio of the shear link damper ($\rho = eV_P/M_P$) was also found to influence the load-bearing, rotation capacity, and plastic overstrength [7–9]. Richards [10], Chao et al. [11], and Ghadami et al. [12] reported that shear link dampers have an overstrength factor of 1.5 to 2, on average. Transverse stiffeners were also proven to be essential in delaying web shear buckling since the failure of shear link dampers usually occurs subsequently [8]. This was later confirmed in the numerical work in [13]. Alternative stiffener configurations were studied in [1, 14–17]. Although shear link dampers are conventionally fabricated from ordinary steel, they can also be made of alternative metallic alloys that could result in more favorable behavior in terms of ductility and energy dissipation [13, 18–24].

To simulate the response of shear link dampers, different analytical models have been developed since the introduction of shear link

* Corresponding author.
E-mail addresses: ahmed_elgammal@stu.scu.edu.cn (A. Elgammal), yasmin_ali@stu.scu.edu.cn (Y. Ali).

https://doi.org/10.1016/j.istruc.2024.107848
Received 15 August 2024; Received in revised form 5 November 2024; Accepted 13 November 2024
Available online 20 November 2024

dampers for the first time. Ricles and Popov [25] modeled shear link dampers as an elastic beam provided with nonlinear hinges at each end. While this model yielded numerically accurate results, its implementation necessitated a complex calibration and programming process [26].

Ramadan and Ghobarah [26] further improved this model using simpler hinges. However, the model was later modified by Richards and Uang [27] in an effort to enhance the predictive accuracy for the behavior of A992 steel link dampers.

Later, a kinematic-isotropic combined hardening restoring force model that can produce hysteretic curves consistent with those of experimentally tested shear link dampers was presented [28,29]. This model is based on hardening parameters that differ with any change in the geometric properties of the shear link damper. To obtain these parameters, trial-and-error was suggested as a method, so that the analytical hysteretic curves match the experimental (or numerical) hysteretic curves [28]. This implies that the hysteretic curve of the shear link damper under consideration should first be available to calibrate and use this model.

Recently, the Vaiana–Rosati model was developed [30,31]. It is a computationally efficient model suitable for complex rate-independent mechanical hysteresis.

Having explored the effectiveness of shear link dampers in mitigating seismic risks, this section now delves into the burgeoning realm of machine learning and its transformative potential within structural engineering. Machine learning, a subset of artificial intelligence, focuses on developing algorithms that enables computers to learn from data for accurate predictions. It encompasses supervised, unsupervised, and reinforcement learning.

Supervised learning involves teaching algorithms using labeled datasets [32]. Structural engineering applications have witnessed the adoption of various machine learning algorithms, including artificial neural networks (ANNs) and evolutionary algorithms [33] such as the genetic algorithm [34].

The aim of developing ANNs is to replicate the functionality of biological neurons. ANNs consist of artificial neurons organized into three tiers: input layer, hidden layer(s), and output layer [32]. For detailed information on neuron behavior and ANN calculations, see [35].

Machine learning has been widely applied in structural engineering [36] for various purposes such as crack prediction [37], low-cycle fatigue estimation [38], axial capacity estimation [36], and seismic assessment of buildings [39].

It is evident that the kinematic-isotropic combined hardening restoring force model [28,29] has a major drawback: its hardening parameters vary from one shear link damper to another. Therefore, they cannot be easily predicted. Furthermore, no specific formulas for calculating these parameters have been derived; they were proposed to be obtained using trial and error in the presence of the original hysteretic curves [28].

Therefore, this research aims to provide an enhanced hysteretic restoring force model and a reliable method to estimate its hardening parameters, in the absence of the original hysteretic curves, based on machine learning.

To this end, three phases were followed in the framework of this research, as shown in Fig. 2. First, a numerical study was conducted on 350 shear link dampers with varying geometric properties, considering material nonlinearity and geometric imperfections, in ANSYS Workbench [40] to shed light on the effect of geometric properties on hysteretic behavior. Second, the obtained hysteretic curves, defined as matrices of displacement and force pairs, were processed using MATLAB [41], and a genetic algorithm was implemented to optimize the hardening parameters for the proposed restoring force model. Third, the optimized hardening parameters, along with the geometric properties of each shear link damper, were utilized to train an ANN in MATLAB [41] to enable the forecasting of these parameters for any other shear link damper based on its geometric properties without the need to first obtain its hysteretic curve. Moreover, blind testing of the proposed model against experimentally tested shear link dampers was carried out to evaluate the accuracy of the ANN.

2. Numerical study

2.1. General

ANSYS Workbench [40] is one of the structural simulation software platforms that uses the finite element method. Consequently, this finite element software was chosen to numerically analyze shear link dampers in this paper. The main steps required to model shear link dampers in this software are precisely described throughout this section.

2.2. Specifications of the shear link damper specimens

A total of 350 transversely stiffened I-shaped shear link damper specimens with compact webs and flanges were analyzed in this paper. All specimens were made of Q345GJ steel, which has a nominal yield stress (σ_y) and an ultimate tensile stress (σ_u) of 345 and 505 MPa, respectively.

To ensure shear yielding occurs before flexure yielding, all specimens were dimensioned such that Eq. (1) was satisfied. Therefore, all specimens had a link length ratio ($\rho = eV_p/M_p$) ranging from 0.54 to 1.59.

Some geometric specifications were kept the same for all specimens. For instance, all specimens shared the same length ($e = 320$ mm), web height ($h_w = 250$ mm), flange thickness ($t_f = 10$ mm), and thickness of the double-sided transverse stiffeners ($t_s = 10$ mm).

On the other hand, different web thicknesses that ranged from 5 to

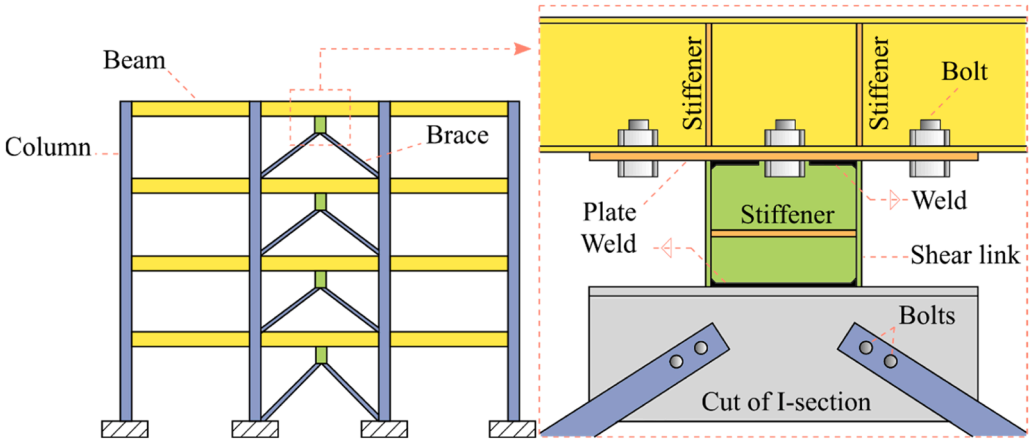

Fig. 1. Eccentrically braced frame with vertical shear links.

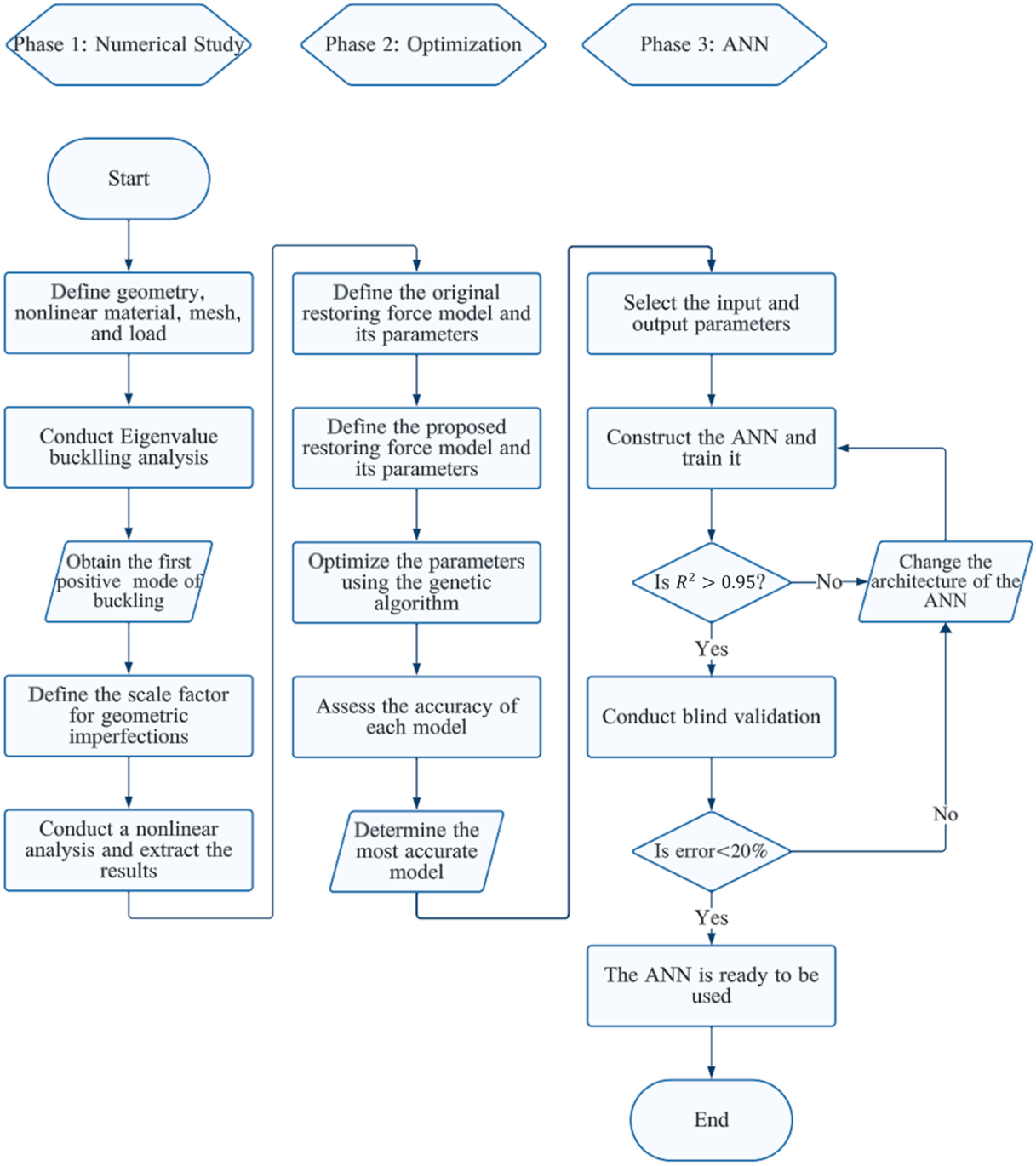

Fig. 2. Flowchart of the methodology adopted in this research.

18 mm were used, thereby causing the web slenderness ratio (h_w/t_w) to vary from 13.88 to 50. This ratio thus satisfies the requirement for highly ductile members set by AISC 341–16 [6].

Five flange widths (b_f) of 100, 110, 120, 130, and 140 mm were also used. As a result, the flange slenderness ratio ($b_f/2t_f$) ranged from 5 to 7, which also satisfies the requirements for moderately ductile members set by AISC 341–16 [6].

Moreover, five web panel aspect ratios (a/h_w) were included in the specimens: 0.64, 0.42, 0.32, 0.25, and 0.21, where a is the stiffener spacing. Fig. 3 presents the values of parameters that were changed in the numerical study.

The labeling scheme of the specimens was taken as $t_w - b_f - a/h_w$ in order for the geometric properties of the cross-section to be easily identified from the label. As an example, the $7 - 140 - 0.25$ specimen has a web thickness (t_w) of 7 mm, a flange width (b_f) of 140 mm, and a web panel aspect ratio (a/h_w) of 0.25 (i.e., a stiffener spacing of 62.5 mm).

2.3. Geometric modeling and mesh sensitivity

A 3-D model for isolated shear link dampers, without the surrounding framing system, was built in ANSYS Workbench [40], as shown in Fig. 4. Web, flanges, and stiffeners of the shear link dampers were represented using the shell element named SHELL181. This element primarily consists of four nodes. Each node of the element is characterized by six degrees of freedom [42]. This element supports applications in

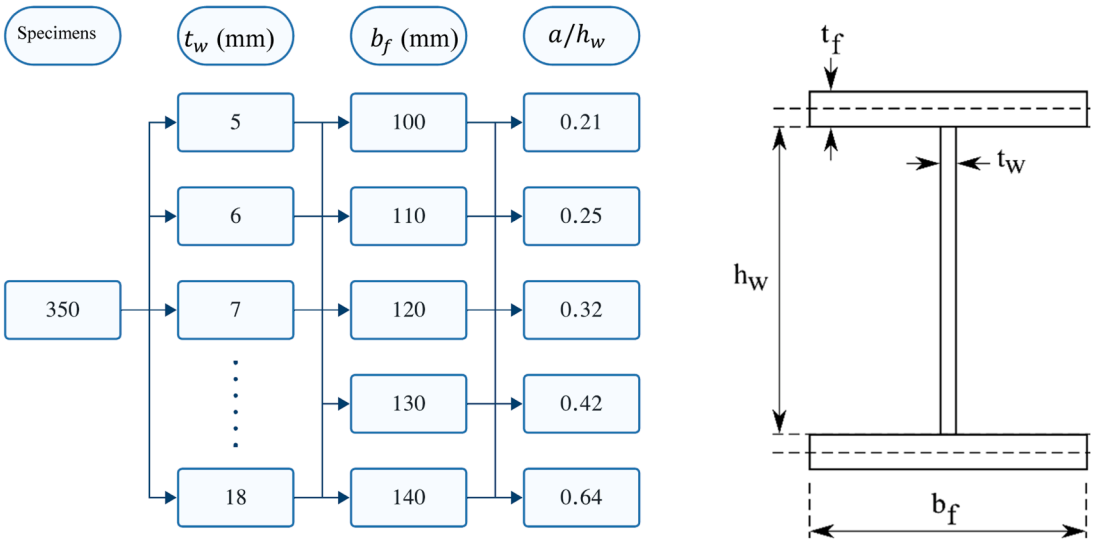

Fig. 3. Parameters of the numerical study.

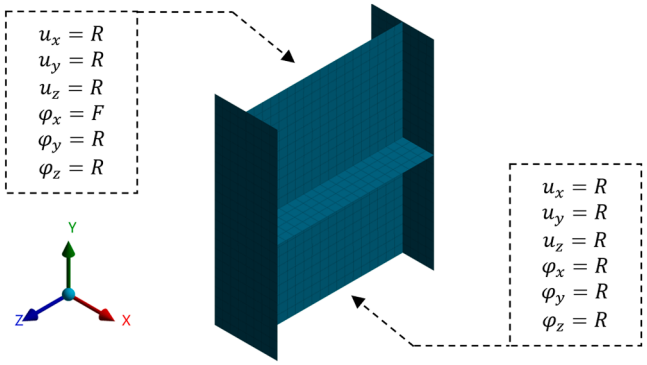

Fig. 4. Finite element model for a typical shear link damper (u: translational degrees of freedom, φ: rotational degrees of freedom, R: restrained, and F: free).

which large nonlinear strains occur, as in shear link dampers [17,43]. Web, flanges, and stiffeners were all merged in the numerical model without considering welds [17,44].

A convergence analysis was conducted to obtain the adequate mesh size on a specimen with a $5 - 100 - 0.21$ configuration, which includes the minimum values for web thickness (t_w) and web panel aspect ratio (a/h_w). This is because this configuration is thought to be highly responsive to changes in mesh size [45]. In detail, finite element analysis of steel plates with transverse stiffeners becomes more sensitive to mesh size when the web panels are reduced in size and the web itself is thinned.

This heightened sensitivity arises due to two primary factors. Firstly, these modifications lead to stress concentrations around the stiffeners and at web panel edges. Accurately capturing the stress distribution in these localized regions necessitates a finer mesh, as a coarse mesh would overlook crucial details and potentially yield inaccurate results. Secondly, thinner webs are more susceptible to shear buckling. Effectively simulating such buckling behavior requires a mesh capable of resolving the buckling deformations. A coarse mesh, in this case, might fail to capture the buckling mode accurately, leading to significant errors in the finite element analysis results.

In essence, with smaller web panels and thinner webs, the critical regions of the plate become more concentrated, demanding a finer mesh for reliable finite element analysis [46,47]. Returning to the initial discussion of the convergence analysis, the specimen under consideration was analyzed nine times. Each time, the number of web panel width divisions was changed from 4 to 20 divisions.

Since it is expected that the largest number of web panel width divisions would be accompanied by the most accurate results, the percentage error in the peak shear force for different web panel width divisions compared to the model with 20 divisions was utilized to evaluate the accuracy of the results. Referring to Fig. 5, it was assumed that 12 web panel width divisions were the optimal case, as it produces a maximum error in the peak shear force not exceeding 1.93 %. This number of web panel width divisions was thus adopted for all specimens under consideration as it minimizes the error corresponding to peak shear force calculation in the numerical analysis.

2.4. Nonlinear modeling of the material

For metallic members subjected to monotonic loading, usually simple isotropic hardening stress-strain curves are used. However, this is not valid for elements subjected to cyclic loading. In general, strain hardening is dependent on the nature of the yield surface after the first yield. For instance, in isotropic hardening, the yield surface equally expands in all directions, which is true in the first few cycles of loading in shear link dampers. On the other hand, the yield surface offsets from its original position while its size is kept constant in the case of kinematic hardening.

This is why kinematic hardening considers the Bauschinger effect that takes place in elements subjected to cyclic loading, unlike isotropic hardening [48]. Due to the important features of isotropic hardening and kinematic hardening in the case of cyclic loading, the model

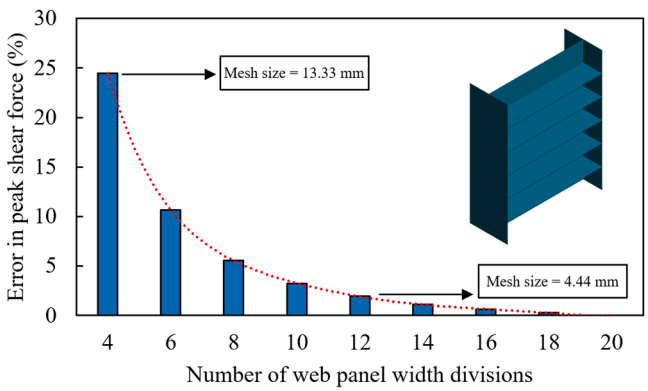

Fig. 5. Sensitivity analysis results.

proposed by Chaboche [49] derived the following formula that relates the isotropic hardening to the kinematic hardening:

$$f(\sigma-\alpha)-\sigma^0=0 \tag{2}$$

where the term $f(\sigma-\alpha)$ represents von Mises stress, while kinematic hardening back stress and isotropic hardening yield stress are denoted by α and σ^0, respectively. The kinematic hardening back stress (α) can be obtained as follows:

$$\alpha=\sum_{k=1}^{n}\alpha_k \tag{3}$$

$$\alpha_k=\frac{C_k}{\gamma_k}\left(1-e^{-\gamma_k\varepsilon^p}\right)+\alpha_0^k e^{-\gamma_k\varepsilon^p} \tag{4}$$

where C_k and γ_k are constants, and their ratio (C_k/γ_k) is equal to the peak stress of the k^{th} back stress; α_0^k is the initial stress of the k^{th} back stress, and ε^p is the plastic strain that can be determined as following:

$$\varepsilon^p=\frac{\varepsilon-\sigma}{E-\varepsilon_p^0} \tag{5}$$

where ε and σ represent the strain and stress for any point on the curve, respectively. E is the modulus of elasticity. ε_p^0 is the negative strain at the point of zero stress.

Regarding the isotropic hardening yield stress (σ^0), Chaboche [49] assumed it as follows:

$$\sigma^0=\sigma|_0+Q_0\varepsilon^p+Q_\infty\left(1-e^{-b\varepsilon^p}\right) \tag{6}$$

where $\sigma|_0$ is the initial tensile yield stress, and Q_0 and Q_∞ are the parameters that characterize the isotropic behavior of the material.

The parameters of Chaboche combined hardening model [49] can be obtained using a calibration methodology, with the aid of experimental cyclic strain tests and monotonic coupon tests. For the Q345GJ steel, Chaboche hardening parameters were taken as reported by Liu et al. [50]. Table 1 includes the non-zero parameters required to model Q345GJ steel using the Chaboche combined hardening model [49]. Fig. 6 depicts the monotonic and cyclic stress-strain curves reported by Liu et al. [50]. No fracture model was included since cyclic fracture is not within the scope of this paper.

2.5. Boundary conditions and cyclic loading protocol

The boundary conditions were taken following the numerical work of [17]. Referring to Fig. 4, both ends of the shear link damper were prevented from rotation ($\varphi_x=\varphi_y=\varphi_z=0$). Moreover, one end of the shear link damper was assumed to have all translational degrees of freedom equal to zero ($u_x=u_y=u_z=0$). Otherwise, the other end of the shear link damper was characterized by two restrained translational degrees of freedom ($u_x=u_y=0$), while the translation in the loading direction was kept free ($u_z\neq 0$).

The deformation-controlled quasi-static cyclic loading protocol, illustrated in Fig. 7, which depends on subjecting the shear link damper to successive rotation angles (γ), was used. The rotation angle (γ) is equal to the relative lateral displacement between the damper ends divided by the length (e). This loading protocol, was adopted by Liu et al. [50].

Table 1
Chaboche hardening parameters for Q345GJ steel [50].

Parameter	Value	Unit
C_1	20000	MPa
γ_1	1000	——
C_2	10000	MPa
γ_2	100	——
C_3	600	MPa
γ_3	20	——
C_4	350	MPa
γ_4	10	——
$\sigma\|_0$	350	MPa

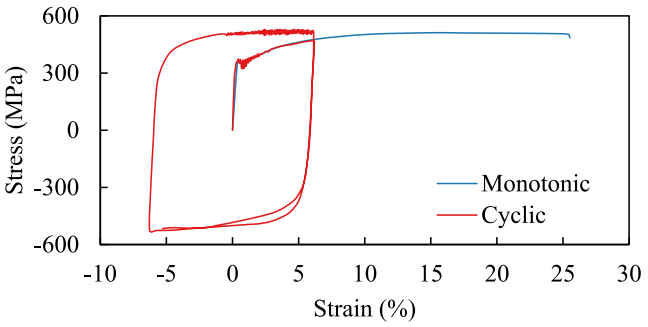

Fig. 6. Monotonic and cyclic stress-strain curves for Q345GJ steel as reported by Liu et al. [50].

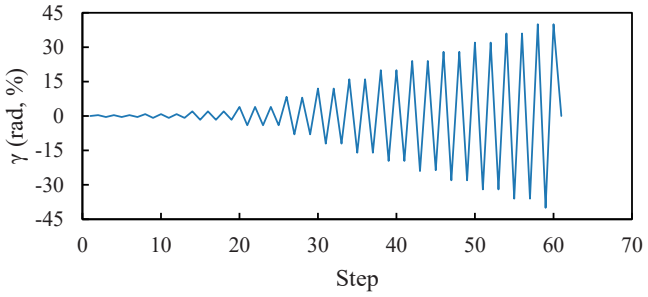

Fig. 7. The cyclic loading protocol adopted by Liu et al. [50].

2.6. Geometric imperfections and residual stresses

To produce a realistic finite element model, geometric imperfections were considered. This was done by carrying out Eigenvalue buckling analysis prior to subjecting the shear link damper to the cyclic loading. Despite the infinite number of buckling modes that the Eigenvalue analysis yields, the general shape of the geometric imperfection was determined based on the first positive buckling mode only [51], as shown in Fig. 8, multiplied by a scale factor. This is because the impact of higher-order buckling modes on the numerical results is negligible [52].

To stick with code provisions, the scale factor was taken as per EN 1993–1-5 [53]. For a rectangular plate of size $b\times h$ (where $b<h$), EN 1993–1-5 [53] sets the value of the scale factor to $b/200$. In most cases, the first buckling mode is characterized by shear buckling of the web

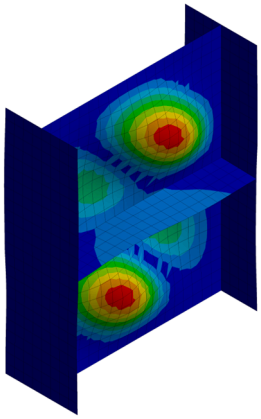

Fig. 8. First Eigenvalue buckling mode of specimen 5 − 100 − 0.64.

plate; thus, in this case, the scale factor is equal to the least of the web height (h_w) or stiffener spacing (a) divided by 200. In contrast, residual stresses were not considered in the numerical model as they do not significantly affect the cyclic behavior of shear link dampers [17,54].

2.7. Validation of the numerical model

This section aims to validate the numerical model developed for shear link dampers by comparing its predictions with the experimental results obtained from tests conducted by Liu et al. [50], and Hjelmstad and Popov [8]. This validation is essential for establishing confidence in the numerical model, as it directly influences the reliability and accuracy of upcoming predictions.

The validation process entails a comprehensive analysis of several critical parameters, including the hysteretic curves, yield shear force (V_y), ultimate shear strength (V_u), elastic stiffness (K_e), and the ratio between cumulative dissipated energy derived from the numerical study and the experimental data (k). Furthermore, congruence in the failure modes observed in both the numerical and experimental studies will be assessed.

The experimental tests utilized in this validation provide insight into the performance of the shear link dampers under various loading histories, which enhances the robustness of the numerical model, ensuring that the model can accurately capture the behavior of the dampers in a range of realistic scenarios, thereby increasing its applicability in practical contexts.

The following sections details the verification studies conducted, presenting the outcomes of the comparisons and discussing the implications of the findings on the reliability of the numerical model.

2.7.1. Validation against Liu et al.'s [50] experimental tests

The accuracy of the numerical model was assessed by establishing ten numerical models for shear link damper specimens experimentally tested by Liu et al. [50] and comparing the results. In Table 2, the geometric properties of the specimens are listed. b_f, t_w, and t_s represent flange width, web thickness, and stiffener thickness, respectively. It is worth noting that the abbreviation "RSL" that appears within the specimen labels signifies "replaceable shear link" and it was adopted from the research by Liu et al. [50].

To maintain consistency and avoid potential confusion, the same labeling scheme was retained for the verification study presented here. All specimens had a cross-sectional depth of 210 mm, a flange thickness (t_f) of 10 mm, and a length (e) of 400 mm. The specimens were made of Q345GJ steel, which was modeled according to the values in Table 1 and subjected to the same cyclic loading protocol shown in Fig. 7.

Fig. 9 shows a comparison between the numerical and experimental hysteretic curves for a sample of the specimens. The numerical results are in good agreement with the experimental results. However, the numerical curves slightly deviate from the experimental ones, exhibiting marginally higher pinching and reduced secant stiffness during the loading phases.

Several factors inherent to numerical modeling can contribute to such discrepancies between numerical and experimental hysteretic curves, even after calibration. Firstly, the material model used might not perfectly capture the intricate behavior of Q345GJ steel under cyclic loading; inaccuracies in representing post-yield stiffness degradation and softening within the model can lead to deviations in the results. Secondly, idealized boundary conditions used in the numerical model may not fully reflect the actual constraints present during the experiment. This can influence the model's energy dissipation and stiffness characteristics. Finally, geometric imperfections presented in the experimental setup, such as slight variations in specimen geometry or boundary conditions, might not be precisely represented in the numerical model using the approach described in Section 2.6, leading to further discrepancies. In such cases, the actual geometric imperfections that the specimens in the experiment truly exhibited should be used in the numerical analysis. But unfortunately, Liu et al. [50] did not report the values of these imperfections.

These discrepancies, however, do not significantly impact the accuracy of the energy dissipation prediction, as the ratio between the cumulative dissipated energy determined from the numerical model and that attained from the experimental curves (κ) ranges from 0.83 to 1.06 for all ten specimens, indicating that the dissipated energy predicted by the numerical model is quite adequate. Table 3 summarizes the yield shear force (V_y), ultimate shear strength (V_u), and elastic stiffness (K_e) of the numerical and experimental testing. The amount of deviation between the experimental and numerical results is less than 13 %, with an average of 4.2 %. Therefore, the proposed modeling technique can produce hysteretic parameters that are almost equal to those of the experimental testing.

Another factor to consider when validating the current numerical model is its capability to simulate the mode of failure of the specimens. Fig. 10 shows a comparison between the failure modes reported by Liu et al. [50] and those obtained from the numerical simulations for a sample of the specimens. The numerical model again proved its efficiency since the failure modes are identical to those obtained from experimental testing in terms of buckling.

Consequently, it is deduced that the proposed numerical model can satisfactorily simulate the cyclic behavior of shear link dampers. However, additional validation was necessary to verify the accuracy of the numerical model when the shear link damper is subjected to a different cyclic loading history. This requires validating the model with a different set of specimens, such as those experimentally tested by Hjelmstad and Popov [8], as discussed in the following section.

2.7.2. Validation against Hjelmstad and Popov's [8] experimental tests

The second validation was carried out based on the experimental test of Hjelmstad and Popov [8]. The selection of this experimental test for validation is justified by its pioneering role in the field of shear link dampers, providing foundational insights that have significantly influenced subsequent research. Hjelmstad and Popov [8] conducted an experimental investigation on fifteen shear link dampers to assess their cyclic performance. However, only specimens 1 and 4 were included in the current verification study. This selection was based on the availability, as Hjelmstad and Popov [8] reported the hysteretic curves and associated failure modes for these two particular specimens only.

Specimens 1 and 4 featured a cross-section of hot-rolled W18 × 40 and each had a length of 711.2 mm. Specimens 1 lacked stiffeners, while specimen 4 was equipped with three equally spaced stiffeners, each with a thickness of 9.53 mm. The specimens were constructed from ASTM A36 steel. The hardening parameters for the Chaboche combined hardening model specific to this steel were not provided by Hjelmstad and Popov [8], so values were obtained from [55] as follows: $\sigma|_0 = 250$ MPa, $C_1 = 2895$ MPa, $\gamma_1 = 20$, $Q_\infty = 80$ MPa, and $b = 2$.

The displacement-controlled cyclic loading protocol comprised a single cycle of 12.7 mm amplitude, followed by two cycles at each increment of 12.7 mm, progressing to amplitudes of 25.4 mm, 38.1 mm,

Table 2
Properties of Liu et al.'s [50] specimens.

Specimen	b_f (mm)	t_w (mm)	a (mm)	t_s (mm)	ρ
RSL−1	130	8	200	6	1.50
RSL−2	100	6	200	6	1.45
RSL−3	160	10	200	3	1.53
RSL−4	130	8	200	4	1.50
RSL−5	130	6	200	6	1.12
RSL−6 −1	130	8	200	6	1.50
RSL−7	130	8	133	6	1.50
RSL−8	115	8	200	6	1.69
RSL−9	105	8	200	6	1.84
RSL−10	130	8	200	4	1.50

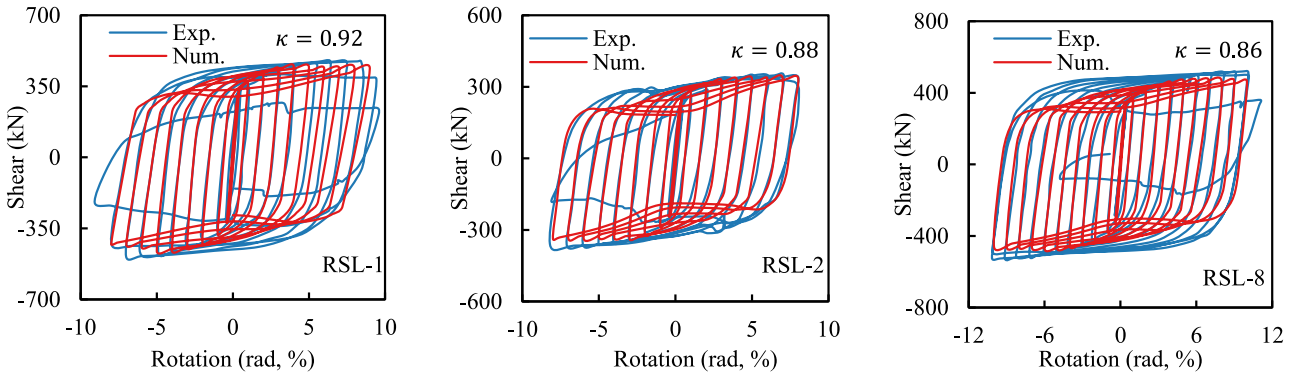

Fig. 9. Hysteretic curves for a sample of the specimens of Liu et al. [50].

Table 3
Comparison of hysteretic parameters between numerical simulations and experimental results from Liu et al. [50] (the units of V_y, V_u, and K_e are kN, kN, and kN/mm, respectively).

Specimen	Exp.			Num.			Num./Exp.		
	V_y	V_u	K_e	V_y	V_u	K_e	V_y	V_u	K_e
RSL−1	362	487	260	348	461	250	0.97	0.95	0.96
RSL−2	272	367	196	262	340	187	0.97	0.93	0.95
RSL−3	453	671	324	448	648	315	0.99	0.97	0.97
RSL−4	362	509	260	353	476	245	0.98	0.94	0.94
RSL−5	272	374	205	265	356	191	0.98	0.96	0.93
RSL−6 −1	362	500	260	347	478	255	0.96	0.96	0.98
RSL−7	362	546	260	359	520	256	0.99	0.96	0.98
RSL−8	362	529	254	349	471	247	0.97	0.89	0.97
RSL−9	362	539	249	350	466	245	0.97	0.87	0.98
RSL−10	362	530	260	356	478	255	0.99	0.91	0.98

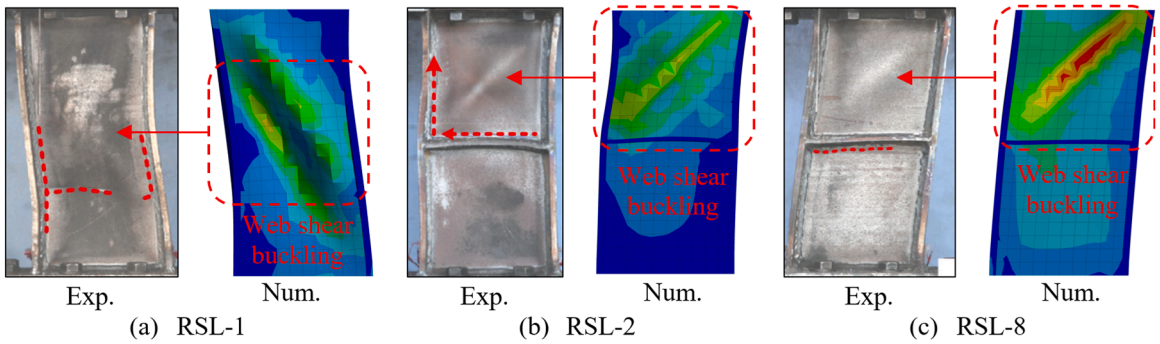

Fig. 10. Failure modes for the specimens of Liu et al. [50] (with contours representing equivalent plastic strain).

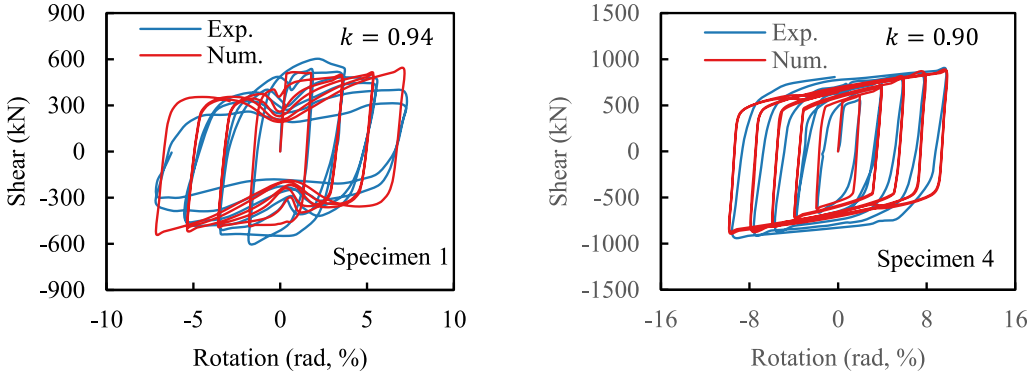

Fig. 11. Hysteretic curves for the specimens of Hjelmstad and Popov [8].

50.8 mm, and so on.

A comparison of the experimental and numerical hysteretic curves is presented in Fig. 11 (noting that experimental and numerical curves are denoted by "Exp." and "Num.", respectively), which indicates a close correlation between the two, despite minor discrepancies, particularly in the unloading segments. This difference can be attributed to the absence of specific hardening parameters necessary for modeling the steel with the Chaboche combined hardening model, as previously mentioned; instead, these parameters were sourced from [55]. As a result, the material model used in the numerical study may not have fully represented the material characteristics tested experimentally.

Despite this, the ratio between the cumulative dissipated energy derived from the numerical simulations to that obtained from the experimental curves (κ) is 0.94 and 0.90 for specimens 1 and 4, respectively. This suggests that these discrepancies had a minimal impact on the overall area enclosed by the hysteresis loops.

It can also be deduced from Table 4 that the ratios of numerical to experimental hysteretic parameters range from 0.88 to 1.08, indicating a reasonable agreement. Additionally, the failure modes identified in the numerical study were consistent with those observed in the experiments, with both specimens failing due to web shear buckling. In the case of specimen 1 (Fig. 12(a)), web shear buckling was observed at the middle height of the web, while specimen 4 (Fig. 12(b)) exhibited concentrated buckling in the end panel.

Based on the validation conducted in this section, it can be concluded that the current numerical model effectively simulates the response of shear link dampers across varying geometric and material properties, as well as under different loading histories. This capability establishes a solid foundation for the core focus of this study, which involves the numerical investigation of an extensive range of shear link dampers.

3. Cyclic performance assessment

Fig. 2 serves as a visual representation of the procedural steps followed in this research. The flowchart delineates the sequential steps taken in the numerical analysis of all 350 specimens. Through this systematic approach, hysteretic curves capturing shear force and rotation angle responses, along with the out-of-plane behavior of web plates, were obtained for each specimen. Subsequently, skeleton curves were derived to facilitate the extraction of the hysteretic parameters. Simultaneously, the cyclic web buckling rotation angle (γ_b) was determined based on the out-of-plane response.

3.1. Mode of failure

Experimental tests on shear link dampers reveal various modes of failure, including flange fracture, web fracture, and weld failure between the web, flanges, or stiffeners [29,50]. These failures predominantly stem from low-cycle fatigue, strongly correlated with load-deformation curves [17,29].

The strong correlation between low-cycle fatigue behavior and load-deformation curves stems from the inherent link between material damage and the evolution of these curves. Cyclic loading induces progressive microstructural damage within the damper material. This damage manifests as a gradual degradation in the stiffness and strength of the damper, which is directly reflected in the hysteretic loops.

As fatigue cracks initiate and propagate, the area enclosed by the loop (representing energy dissipation) typically decreases, signifying a reduction in the damper's energy absorption capacity. Conversely, the peak load and displacement values may also change, indicating a loss of peak strength and deformability. Therefore, by analyzing the hysteretic behavior through load-displacement curves, one can gain valuable insights into the low-cycle fatigue performance and potential damage accumulation within the shear link damper.

Illustrated in Fig. 13, the evolutionary progression of low-cycle fatigue comprises four stages: elastic, hardening, stabilization, and failure. Initially, the panel remains elastic with a linear load-deformation curve, denoting high stiffness. Upon surpassing a threshold, yielding initiates, transitioning the damper into the hardening phase, marked by increased restoring shear force. With progressive plastic deformation, the restoring force saturates, indicating the stabilization phase. Ultimately, significant degradation in restoring force signifies damper failure [29].

In the numerical analysis, it was observed that all the specimens underwent a consistent four-stage development process in terms of the relationship between the restoring shear force and rotation angle, as depicted in Fig. 14 for one of the specimens, namely specimen 5–100-0.64.

Nevertheless, since cyclic fracture was not included in the numerical model, the final fracture of the shear link damper cannot be simulated. As a result, the failure mode of the specimen can be evaluated according to the deformed shape at the end of the stabilization phase and the beginning of the failure phase [17].

Fig. 15 shows the deformed shape of specimen 5 −100 −0.64 at each of the four stages of low-cycle fatigue, along with a plot of the von Mises stress distribution. At the elastic phase, it is seen that the maximum stress acting on the shear link damper is below the tensile yield stress of the material (345 MPa). At the hardening phase, the web exhibited full yielding, which is indicative of shear yielding, in addition to the formation of plastic hinges at the roots of the flanges.

At the stabilization stage, the shear link damper was subjected to significant web shear buckling in addition to minor compression buckling of the flanges. Larger portions of the flanges in this stage exceeded the material tensile yield stress (345 MPa). At the final failure, the shear link damper is excessively deformed; the web is subjected to large out-of-plane displacements; and at the same time, the flanges suffered from high compression buckling. This is due to the axial constraints at the upper and lower ends of the shear link damper [56].

To investigate the principal tensile strain distribution in the web, three mesh elements along the diagonal line of the web panel of specimen 5 − 100 − 0.64 were considered at the onset of reaching the ultimate shear strength, as shown in Fig. 16. This location along the diagonal best represents the anticipated principal tensile strain direction within the web since shear loading typically induces principal strains along diagonal directions.

It is seen that the three considered points maintained their principal tensile strain at an angle of $40^\circ < \alpha < 45^\circ$. This finding illustrates that a tension field is diagonally developed during the post-buckling phase. This is consistent with the observations of Xu et al. [29].

3.2. Yield shear strength

Plastic shear capacity (V_P) can be calculated following the recommendations of ANSI/AISC 341–16 [6] as follows:

Table 4
Comparison of hysteretic parameters between numerical simulations and experimental results from Hjelmstad and Popov [8] (the units of V_y, V_u, and K_e are kN, kN, and kN/mm, respectively).

Specimen	Exp.			Num.			Num./Exp.		
	V_y	V_u	K_e	V_y	V_u	K_e	V_y	V_u	K_e
1	383	603	130	417	533	129	1.08	0.88	0.99
4	493	891	132	532	864	141	1.07	0.97	1.06

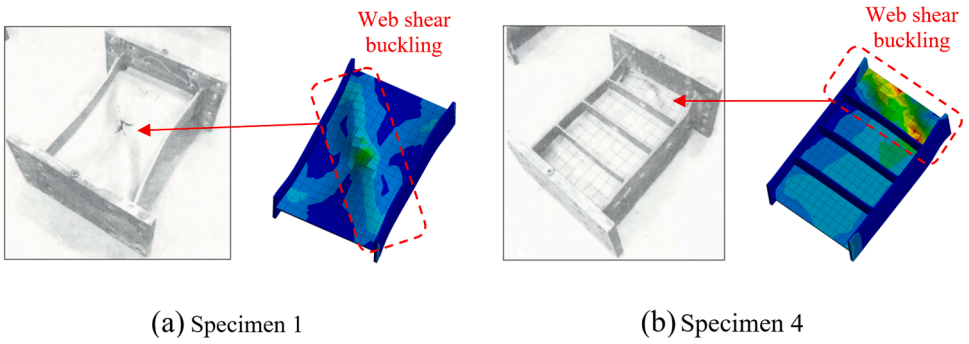

Fig. 12. Failure modes for the specimens of Hjelmstad and Popov [8] (with contours representing equivalent plastic strain).

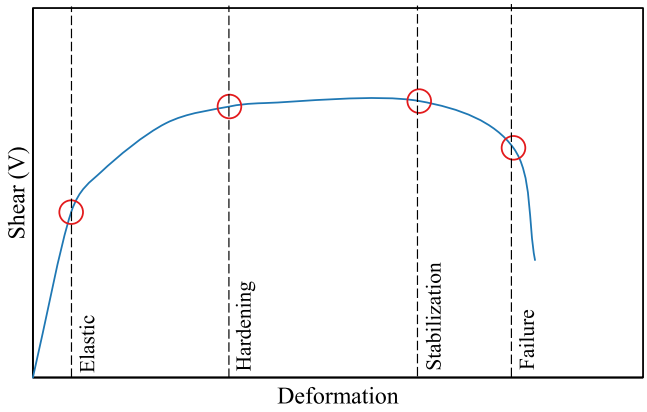

Fig. 13. Progression of the low-cycle fatigue.

$$V_P = 0.6\sigma_y h_w t_w \tag{7}$$

Numerous studies suggest potential deviations between the actual yield shear strength (V_y) and the code-predicted plastic shear capacity (V_P) [17,57], although some findings contradict this notion. Hence, this investigation aims to address these inconsistencies by examining the efficacy of the existing formula outlined in ANSI/AISC 341–16 [6] in estimating (V_y).

Fig. 17(a) depicts a comparison between the yield shear strength (V_y) and plastic shear capacity (V_P) for all 350 specimens. The yield shear strength (V_y) was determined using the graphical method of angle bisector [28,29], as illustrated in Fig. 17(b). The plot reveals closely clustered points for yield shear strength (V_y) and plastic shear capacity (V_p) with differences generally less than 20 % of the ideal value ($V_y = V_p$). A curve fitting operation was carried out and.

Eq. (8) was produced to predict the yield shear strength (V_y) based on the plastic shear capacity (V_p). In Fig. 17(a), the fitted linear trendline (black solid line) achieves a coefficient of determination (R^2) of 0.9998, indicating an excellent fit.

$$V_y = 1.15V_P \tag{8}$$

3.3. Plastic overstrength

Plastic overstrength (Ω) in shear link dampers refers to the ability to withstand shear forces beyond the theoretical yield strength. Eq. (9) can be used to determine the plastic overstrength (Ω) for shear. Although it is assumed in ANSI/AISC 341–16 [6] to be 1.5, relevant studies have shown that it can reach much higher values [58,59]. In contrast, other studies, such as that by Sim et al. [60], have indicated that the overstrength factor for shear can, in some cases, fall below the ANSI/AISC 341–16 [6] recommended value of 1.5. Sim et al. [60] found that the overstrength factor is influenced by various parameters, including material strength, the ratio of actual tensile to yield stresses, localized flange bending in the shear link damper, and the thickness ratios of the flange and web. Given these findings, and upon initial inspection of Fig. 18, showing the relationship between the plastic overstrength (Ω) for shear and different geometric properties of the 350 shear link dampers under study, it is evident that the overstrength factors obtained in the current numerical study are indeed lower than the ANSI/AISC 341–16 [6] benchmark. This suggests that the 1.5 value may be more of a general guideline rather than a definitive value, with the actual overstrength factor potentially requiring case-specific evaluation through detailed analysis, as demonstrated in the current study.

$$\Omega = V_u / V_y \tag{9}$$

Fig. 18(a) illustrates that increasing the web slenderness ratio (h_w/t_w) correlates with an increase in plastic overstrength (Ω). Specifically,

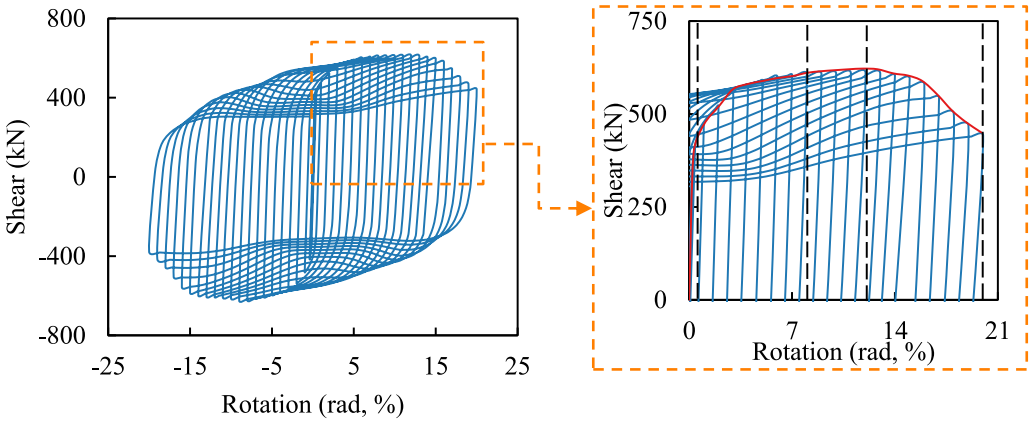

Fig. 14. Hysteretic response of specimen 5 – 100 – 0.64.

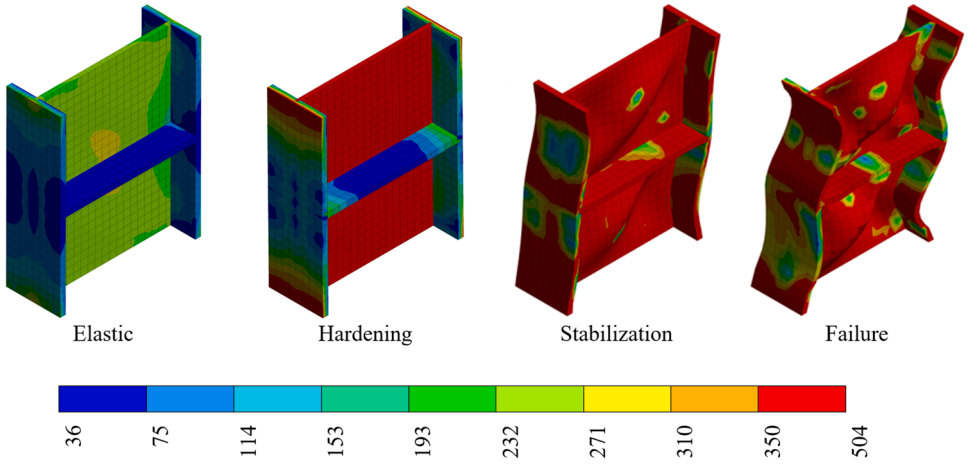

Fig. 15. Distribution of von Mises stress at each stage of low-cycle fatigue for specimen 5 − 100 − 0.64 (unit: MPa).

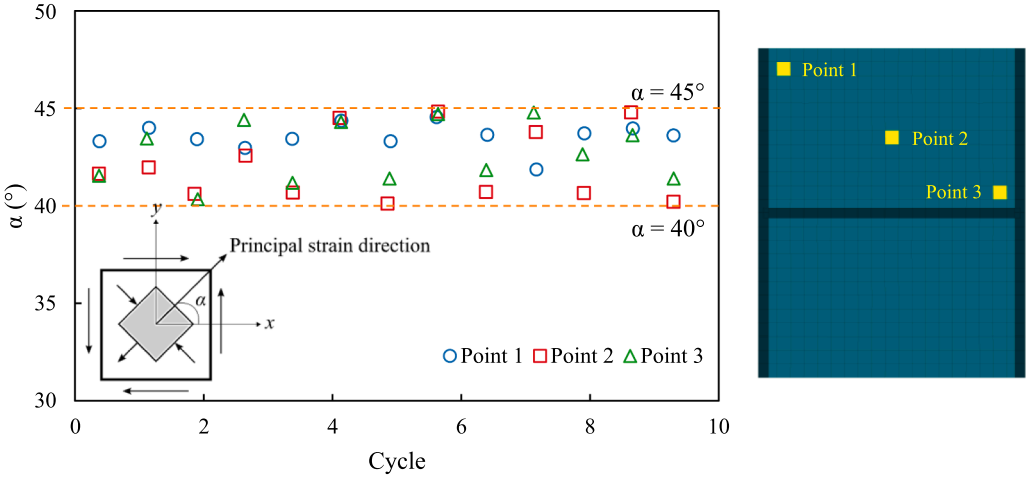

Fig. 16. Variation of principal tensile strain angle (α) with the cycle number for specimen 5 − 100 − 0.64.

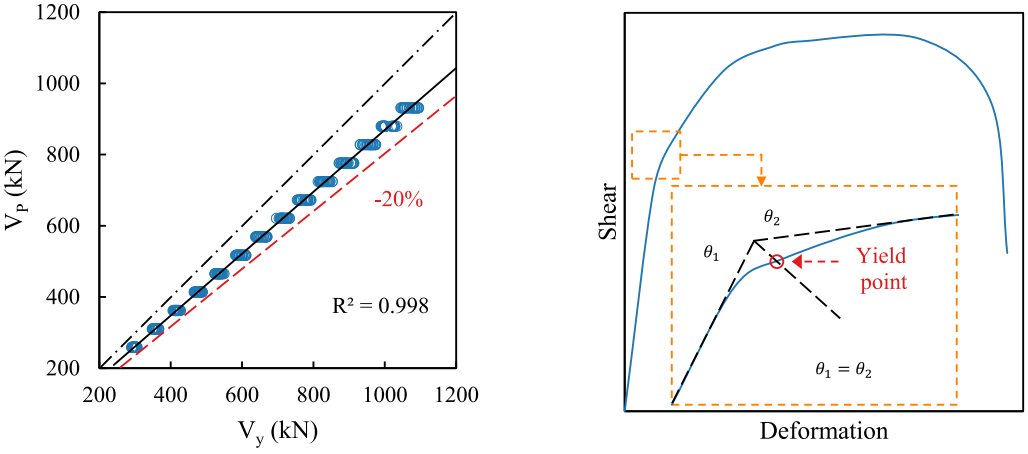

(a) Prediction of yield shear strength (b) Angle bisector approach

Fig. 17. Comparison between yield shear strength (V_y) and plastic shear capacity (V_P).

raising the web slenderness ratio from 13.88 to 50 led to an average 6.6 % increase in Ω. Conversely, reducing the ratio below 20 showed no significant impact on Ω.

In the realm of statistics, the Pearson correlation coefficient (r) serves as a measure of the linear correlation between two variables, denoted as x and y for a certain number of paired data points (n). Eq. (10) can be used to determine that coefficient, confined within the range of −1 to + 1, where + 1 signifies a perfect positive linear correlation, 0 indicates no correlation, and −1 denotes a perfect negative linear correlation. To sum up, the magnitude of (r) reflects the strength of the relationship,

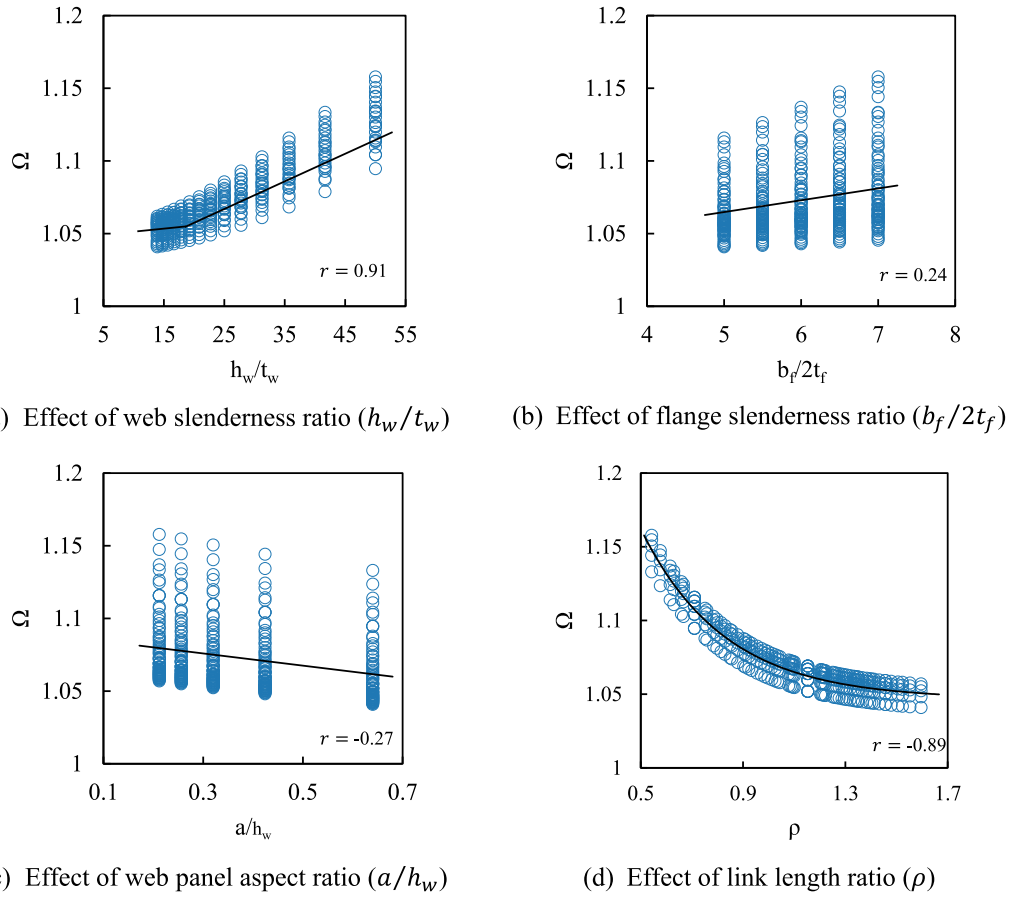

(a) Effect of web slenderness ratio (h_w/t_w)

(b) Effect of flange slenderness ratio ($b_f/2t_f$)

(c) Effect of web panel aspect ratio (a/h_w)

(d) Effect of link length ratio (ρ)

Fig. 18. Plastic overstrength (Ω) for shear.

with values close to the extremes indicating a stronger relationship.

$$r = \frac{n(\sum xy) - (\sum x)(\sum y)}{\sqrt{\left[n(\sum x^2) - (\sum x)^2\right]\left[n(\sum y^2) - (\sum y)^2\right]}} \quad (10)$$

The Pearson correlation coefficient (r) indicates a strong positive relationship (exceeding 0.5) between the web slenderness ratio and plastic overstrength for shear, highlighting the latter's dependency on the former. In Fig. 18(b), variations in plastic overstrength (Ω) with different flange slenderness ratios ($b_f/2t_f$) are depicted. Increasing the ratio by 40 % (from 5 to 7) yielded only a modest average increase in Ω of 1.4 %. With a Pearson correlation coefficient (r) below 0.5, the relationship appears weak, suggesting that practical changes in flange slenderness have minimal impact on shear link dampers' plastic overstrength.

Fig. 18(c) illustrates the correlation between plastic overstrength (Ω) and web panel aspect ratio (a/h_w). As the aspect ratio increases from 0.21 to 0.64, the average Ω decreases marginally from 1.077 to 1.063. However, with an r value below 0.5, the relationship appears weak. This contradicts findings in [43], likely due to the lower web panel aspect ratios used in the current study. Fig. 18(d) indicates an inverse relationship between plastic overstrength (Ω) and the link length ratio ($\rho = eV_P/M_P$). Notably, Ω stabilizes once the ratio surpasses 1.2. The strong relationship between these parameters, indicated by a high Pearson correlation coefficient (r), is evident upon examination.

3.4. Cyclic web shear buckling rotation angle

Cyclic web shear buckling, a pivotal concern in shear link damper design, refers to repetitive out-of-plane instabilities experienced by the web due to cyclic loading, often leading to subsequent failure [28,50]. Fig. 19(a) displays the out-of-plane displacements of specimen.

5–100-0.64's web under cyclic loading. Initially, displacements were minimal, increasing rapidly upon yielding onset, facilitating easier deformation. Subsequent web shear buckling led to severe displacement escalation. Displacements continue to rise rapidly with increasing rotation angle (γ) until approximately $\gamma = 0.13$ rad, after which the rate of increase diminishes notably. This abrupt change stems from material hardening, resisting further deformation and reducing the rate of displacement change.

Zhu et al. [61] recently proposed assuming shear buckling occurs when the web experiences an out-of-plane displacement equal to 10 % of the web thickness (t_w), allowing for neat identification of the corresponding rotation angle (γ_b). For specimen 5–100-0.64, for example, the cyclic web shear buckling rotation angle (γ_b) was found to be 0.05 rad. Fig. 19(b) combines the skeleton curve of specimen 5–100-0.64 with the out-of-plane web response, with the abscissa representing the rotation angle (γ). Following cyclic web shear buckling, the shear link damper maintained the ability to resist higher shear forces, as evident in the hardening plateau, which is consistent with the findings in [49].

A sensitivity analysis was employed to investigate the impact of geometrical parameter variations on the cyclic web shear buckling rotation angle (γ_b). For this purpose, the one-variable-at-a-time (viz., OVAT) analysis was used [62,63]. It is a simple and straightforward approach to evaluating the impact of individual variables on a system, so non-influential factors can be preliminarily screened. Fig. 20 displays the results of the one-variable-at-a-time (OVAT) analysis through tornado charts, aiming to identify the most influential factors on the cyclic web shear buckling rotation angle (γ_b).

The vertical dividing line represents the mean $\gamma_b$with geometric properties set to their optimal values. Red and blue bars for each variable indicate γ_b values obtained by individually altering the meta vari-

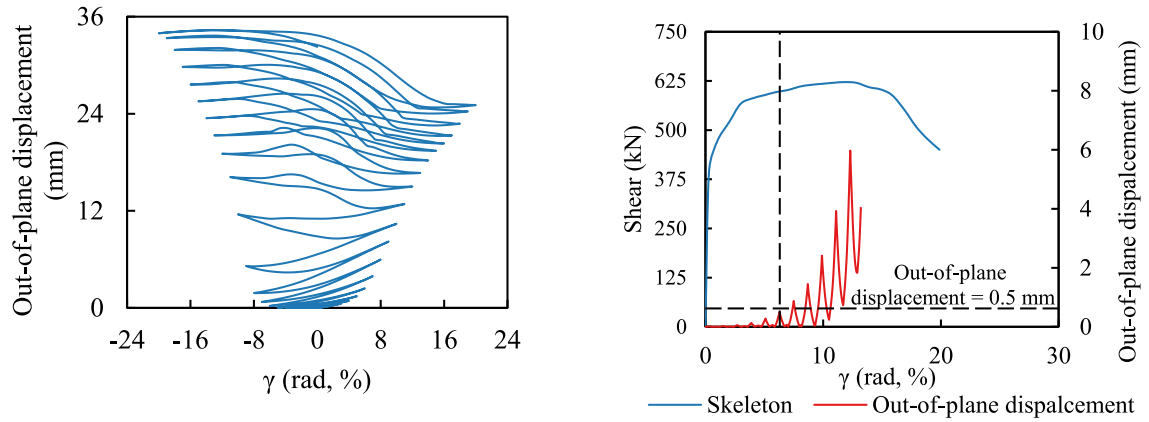

(a) Out-of-plane cyclic displacements of the web (b) Effect of cyclic web shear buckling on the skeleton curve

Fig. 19. Cyclic web shear buckling of specimen 5 − 100 − 0.64.

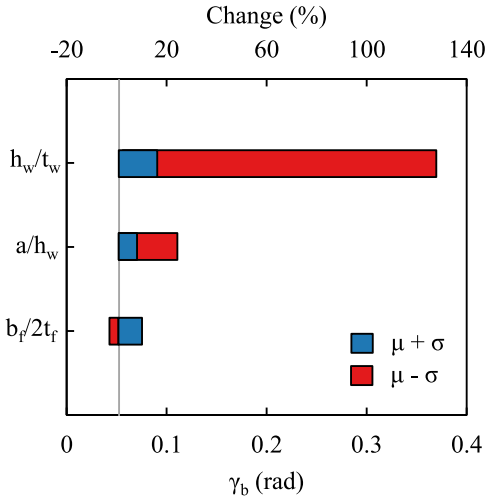

Fig. 20. Tornado chart showing the effect of changing each meta parameter individually ($\pm\sigma$) on the mean cyclic web shear buckling rotation angle (γ_b).

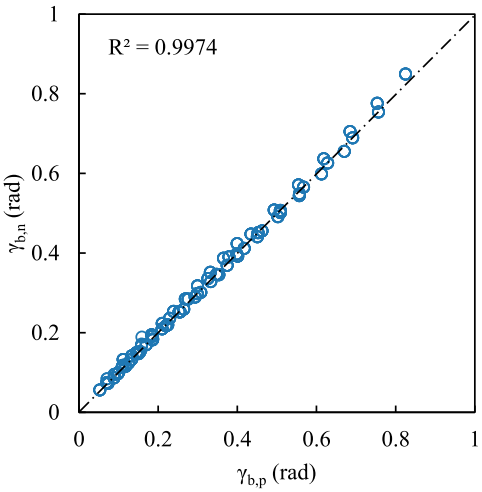

Fig. 21. Cyclic web shear buckling rotation angles obtained numerically and analytically.

able by $\pm\sigma$ (standard deviation) relative to μ (mean). The full bar length represents a variable's relative effect on γ_b. Variables are arranged vertically based on bar length, resembling a tornado shape. The upper horizontal axis depicts the percent change in γ_b relative to the mean. The link length ratio (ρ) was excluded from the analysis as it could not be independently changed without altering other geometric properties.

Fig. 20 indicates that the flange slenderness ratio ($b_f/2t_f$) has the least impact on the cyclic web shear buckling rotation angle (γ_b), while the web slenderness ratio (h_w/t_w) and web panel aspect ratio (a/h_w) are the most influential parameters. Consequently, a nonlinear least-square regression analysis, conducted using MATLAB [41] on the results of 350 specimens, derived Eq. (11) relating γ_b to the two influential parameters.

Fig. 21 compares the γ_b values obtained from the numerical study ($\gamma_{b,n}$)) with those predicted by Eq. (11) ($\gamma_{b,p}$). The derived formula adequately predicts γ_b with insignificant deviations, and it boasts a coefficient of determination (R^2) of 0.9974, indicating an exceptionally high level of goodness of fit.

$$\gamma_b = 20.42(h_w/t_w)^{-1.58}(a/h_w)^{-0.63} \tag{11}$$

3.5. Elastic stiffness

Elastic stiffness (K_e) of shear link dampers can be analytically estimated in accordance with the beam theory and FEMA 356 [64] as follows:

$$K_e = \frac{1}{1/K_s + 1/K_f} \tag{12}$$

$$K_s = \frac{Gh_wt_w}{e} \tag{13}$$

$$K_f = \frac{12EI}{e^3} \tag{14}$$

where K_s is the shear stiffness, K_f is the flexural stiffness, G is the shear modulus, and I is the moment of inertia.

To ensure the applicability of the aforementioned formulas for calculating the elastic stiffness of shear link dampers, the scatter plot presented in Fig. 22 is referred to. In this plot, the analytical values of K_e ($K_{e,a}$) are plotted on the x-axis, while the corresponding values obtained from numerical analysis ($K_{e,n}$) are depicted on the y-axis.

It is evident from the scatter plot that there are deviations between the analytical and numerical estimations, as the data points do not lie precisely on the identity line. In other words, the analytical approach underestimates the actual elastic stiffness since all scatter points lie in the upper half of the figure above the identity line. Although those deviations are moderate, they indicate that the current formulas in FEMA 356 [64]

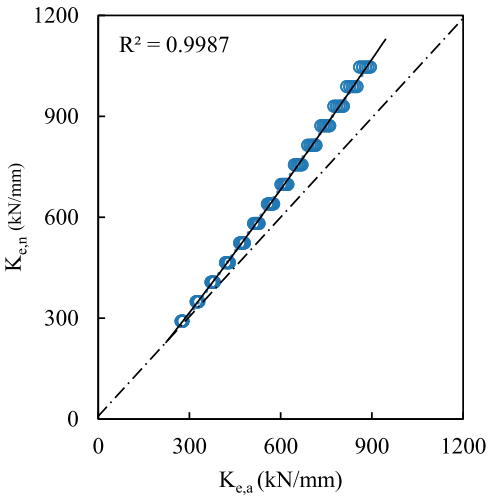

Fig. 22. Cyclic web shear buckling rotation angles obtained numerically and analytically.

may not fully capture the specific characteristics of shear link dampers.

To improve the accuracy and reliability of these analytical predictions, it is recommended to modify the existing formulas to better align with the observed behavior of shear link dampers. In this regard, a univariable nonlinear regression analysis was performed, revealing that the actual elastic stiffness of shear link dampers ($K_{e,\mathrm{mod}}$) adheres to the power law described by Eq. (15), where K_e is the elastic stiffness obtained by Eq. (12).

$$K_{e,\mathrm{mod}} = 0.57{K_e}^{1.108} \tag{15}$$

The high coefficient of determination of this equation ($R^2 = 0.998$) suggests a strong correlation and validates the proposed modification. By adopting this refined approach, more precise and reliable results can be obtained for the elastic stiffness of shear link dampers.

4. Analytical modeling

Due to the work-hardening feature present in nearly all steel grades, analytical simulation of hysteretic response encounters challenges, given the involvement of both isotropic and kinematic hardening. Hence, a kinematic-isotropic combined hardening restoring force model, as suggested in earlier studies [28,29] and following the work of Chaboche et al. [49,65], was utilized as a start point.

In this model's basic framework, the lateral displacement (δ) of the shear link damper comprises elastic (δ_e) and plastic (δ_p) components. During the elastic phase ($\delta \le \delta_y$, where δ_y is the yield shear displacement), the restoring shear force (F) can be estimated as follows:

$$F = K_e\delta \tag{16}$$

For the post-yield phases, the restoring shear force (V) increases due to the material work-hardening. Hence, the evolution of the load-displacement hysteretic curve (F) can be expressed based on the concept of the yield surface as follows:

$$F = |V - X| - R - V_0 = 0 \tag{17}$$

where X is a kinematic hardening parameter representing the translation of the yield surface, R is an isotropic hardening parameter representing the expansion of the yield surface, and V_0 is the initial size of the yield surface, which is equivalent to the plastic shear capacity (V_P). The normality rule defines the rate of change of the plastic displacements ($d\delta_p$) as follows:

$$d\delta_p = d\lambda\frac{\partial F}{\partial V} = d\lambda sign(V - X) \tag{18}$$

where *sign* is the signum function. The kinematic and isotropic hardening parameters can be given in differential forms (i.e., dX and dR, respectively) as follows:

$$dX = C_X[sign(\sigma - X)Q_X - X]d\lambda \tag{19}$$

$$dR = C_R[Q_R - R]d\lambda \tag{20}$$

where C_X and C_R are constants, whereas Q_X and Q_R are the asymptotic values of the cyclic refreshing of the kinematic and isotropic hardening parameters, respectively. For simplicity, the kinematic and isotropic hardening parameters can be exponentially represented as follows:

$$X = Q_X\left(1 - e^{-\beta_X\delta_p}\right) \tag{21}$$

$$R = Q_R\left(1 - e^{-\beta_R\delta_p}\right) \tag{22}$$

where β_X and β_R denote isotropic and kinematic hardening variables. Thereafter, the evolution of the load-displacement hysteretic curve in the post-yield stage (F) can be obtained by summing V_0, X, and R as follows:

$$F = V_0 + X + R \tag{23}$$

However, in this paper, a modified hysteretic restoring force model is presented by making some adjustments to the original restoring force model introduced in this section. First of all, in the elastic phase, the elastic stiffness that defines the linear load-displacement relationship in Eq. (16) is replaced by the modified elastic stiffness ($K_{e,\mathrm{mod}}$) obtained by Eq. (15). This is to ensure that the analytical representation of the shear link dampers response in the elastic phase is accurate enough, as discussed in Section 3.5.

Furthermore, it is demonstrated in Section 3.2 that shear link dampers under consideration yielded at a shear strength higher than the plastic shear capacity. Thereupon, the initial size of the yield surface (V_0) is suggested to be replaced by the yield shear strength of Eq. (8). The inclusion of the calibrated yield shear strength in the modified hysteretic restoring force model enhances accuracy by providing a flexible scaling factor for the initial size of the yield surface (V_0). This adjustment allows the model to better fit experimental data by accounting for variations in material properties and conditions that may cause the actual yield surface to exceed the nominal value.

According to the work of Liu and Liu [66], the used Q345GJ steel grade mostly does not exhibit isotropic hardening behavior. Consequently, the isotropic hardening part (R) is removed in the proposed hysteretic model for simplicity. To this end, the proposed hysteretic restoring force model becomes as follows:

$$F = \begin{cases} K_{e,\mathrm{mod}}\delta_e \text{for} \delta \le \delta_y \\ V_y + X \text{for} \delta > \delta_y \end{cases} \tag{24}$$

where δ_y is the yield displacement that can be obtained in terms of the yield shear strength (V_y) and elastic stiffness ($K_{e,\mathrm{mod}}$) as follows:

$$\delta_y = \frac{V_y}{K_{e,\mathrm{mod}}} \tag{25}$$

As seen in Eq. (24), the proposed hysteretic restoring force model is characterized by two primary branches: an initial linear elastic phase ($\delta \le \delta_y$) and a subsequent kinematic hardening phase ($\delta > \delta_y$). The latter is modeled using an exponential function, as shown in Eq. (21). However, due to the nature of the calibrated parameters Q_X and β_X that define the kinematic hardening phase, as detailed in the following sections, the resulting load-displacement curve in the hardening phase exhibits a mild smoothness that closely approximates a straight line, distinguishing this model as effectively bilinear.

While more complex models, such as those developed by Vaiana et al. [67,68], can provide highly detailed curvilinear representations,

the bilinear model is selected here due to its balance between accuracy and computational efficiency. This simplification facilitates calibration and implementation without substantial sacrifice of accuracy in predicting damper behavior, particularly for engineering applications requiring practical and reliable performance models.

It should be noted that the original model does not predict the ultimate load-carrying capacity or the specific point on the hysteretic curve where the shear link damper begins to exhibit strength deterioration. To address this limitation in the proposed analytical model, the damper's response is assumed to terminate when the rotation angle reaches the cyclic web shear buckling rotation angle, as estimated by Eq. (11).

This assumption is based on previous experimental findings [28,50], which indicate that shear link dampers typically fail upon reaching this rotation angle. Terminating the hysteretic curve at this point is logical, as experimental evidence suggests that, beyond this angle, the area enclosed by the hysteresis loops begins to decrease, signifying a loss in energy dissipation and structural integrity.

5. Estimating hardening parameters via machine learning

The proposed restoring force model requires trial and error to determine the values of its two hardening parameters: Q_R and β_R. Initially assumed values are adjusted until the model produces a hysteretic curve, using Eq. (24), that matches the original one. However, obtaining actual hysteretic curves and determining parameter values lack specific methodologies.

To address this, a machine learning-based approach using ANNs was adopted to predict these parameters based on the geometric properties. This approach requires dataset training, achieved through genetic algorithm optimization on 350 specimens, yielding optimized parameter values. This enriched dataset formed the basis for ANN training.

5.1. Genetic algorithm optimization

Inspired by natural selection, genetic algorithms iteratively search for optimal solutions through a population of evolving individuals. These individuals undergo crossover and mutation to produce offspring, with fitter individuals having a higher chance of selection for reproduction [69].

In MATLAB [41], a genetic algorithm was utilized to find optimal parameter values. Initial generation members searched for these values, terminating if accuracy criteria were satisfied; otherwise, subsequent generations were generated via crossover and mutation.

The objective function, defined as the mean squared error (*MSE*), guided the search for the optimal solution. The goal was to determine, for each shear link damper, the hardening parameters that minimize the sum of squared area differences between numerical and analytical hysteretic curves in each cycle (i) [36], obtained as follows:

$$MSE = \sum_{i=1}^{N} \xi_i (A_{ni} - A_{ai})^2 \tag{26}$$

where ξ_i is the normalized weight for each cycle, which was assumed to be 1 for simplicity [70], and A_n and A_a are, respectively, the areas of each loop of the numerical and analytically predicted hysteretic curves. The optimal hardening parameter values for each shear link damper were determined, forming the basis for the ANN training process alongside the geometric properties of each damper.

For instance, in specimen 5–100-0.64, these optimal parameters were used in Eq. (24) to generate a hysteretic curve aligning with numerical results (Fig. 23(a)). Additionally, the original model's hysteretic curve was plotted for comparison. Overall, the original model's curve appeared lower than the other two. Conversely, the proposed model, exhibited similar traits to the numerical, suggesting its superior ability to simulate the hysteretic response.

Fig. 23(b) illustrates the variation of mean squared error (*MSE*) with the evolution of genetic algorithm generations. Both the original and proposed models display a decreasing trend in *MSE*, with the proposed model showing slightly lower values. Furthermore, in Fig. 23(c), the absolute percentage error in yield shear strength (V_y), peak shear strength (V_u), and cumulative dissipated energy (U_c) between the numerical and model-generated hysteretic curves is presented.

The proposed model demonstrates more efficient simulation, with errors ranging from 5.3 to 7.2 %, notably lower than those of the original model. Accordingly, the hardening parameters obtained through genetic algorithm optimization can then be used to train the ANN.

5.2. Artificial neural network (ANN)

5.2.1. Architecture of the artificial neural network (ANN)

The ANN model consists of interconnected neurons arranged in input, hidden, and output layers. Each neuron connects to others via weighted links, with biases added to the weighted sum of inputs. The neuron's output is produced through an activation function, such as the logistic sigmoid, hyperbolic tangent, or simple linear function [71,72].

In MATLAB [41], a feedforward perceptron ANN with backpropagation was developed to predict hardening parameters (Fig. 24) [63,73]. Bayesian Regularization was chosen to prevent overfitting, as it combines error minimization with weight regularization, enhancing the model's generalization. This approach is particularly effective for the relatively small dataset of 350 specimens, dynamically balancing data fit with model simplicity to ensure reliable performance on new data [74].

The ANN model's inputs included six geometric properties of the shear link damper: web slenderness ratio (h_w/t_w), web thickness (t_w), flange slenderness ratio ($b_f/2t_f$), flange width (b_f), web panel aspect ratio (a/h_w), and length ratio (ρ). This comprehensive inclusion of all geometric properties aims to maximize accuracy by capturing the complex interactions between them, which are crucial for accurately modeling the damper's behavior. Although feature selection techniques are available, including all variables ensures that no potentially significant factor is overlooked.

The ANN outputs two hardening parameters Q_R and β_R, with both inputs and outputs normalized to the range [0,1]. Normalization is critical for efficient ANN operation, as it stabilizes training, speeds up convergence, and mitigates issues arising from differing data scales, thus enhancing model performance. Typically, datasets are divided into training, validation, and testing sets; however, when using Bayesian Regularization, the data is often split only into training and testing sets.

This approach leverages the algorithm's built-in regularization to control model complexity, minimizing both squared errors and weights, thereby reducing overfitting without needing a separate validation set. Using more data for training improves learning, especially valuable for smaller datasets, and ensures reliable evaluation on the test set. [75].

Since there is no universally applicable proportion for data division, the ANN was trained and tested using 80 % and 20 % of the data, respectively. This approach maximalizes the training data available while reserving sufficient data for reliable evaluation, achieving a balance between model training and generalization capacity [76]. The number of epochs was set at 1000 to ensure network convergence [77]. A single hidden layer was chosen to keep the model simple yet effective, leveraging the universal approximation theorem, which states that a single hidden layer can approximate any continuous function if enough neurons are used [78]. The hyperbolic tangent activation function was applied in the hidden layer, and a simple linear function in the output layer [63].

To determine the optimal number of neurons in the hidden layer, tests were conducted with neuron counts from 5 to 40, in increments of 5. The configuration with the lowest MSE was selected as optimal. This method ensures a balanced model with sufficient complexity while minimizing overfitting risks. Fig. 25 shows the relationship between neuron count and MSE As depicted, the training MSE decreases sharply with an increasing number of neurons up to around 10 neurons, then

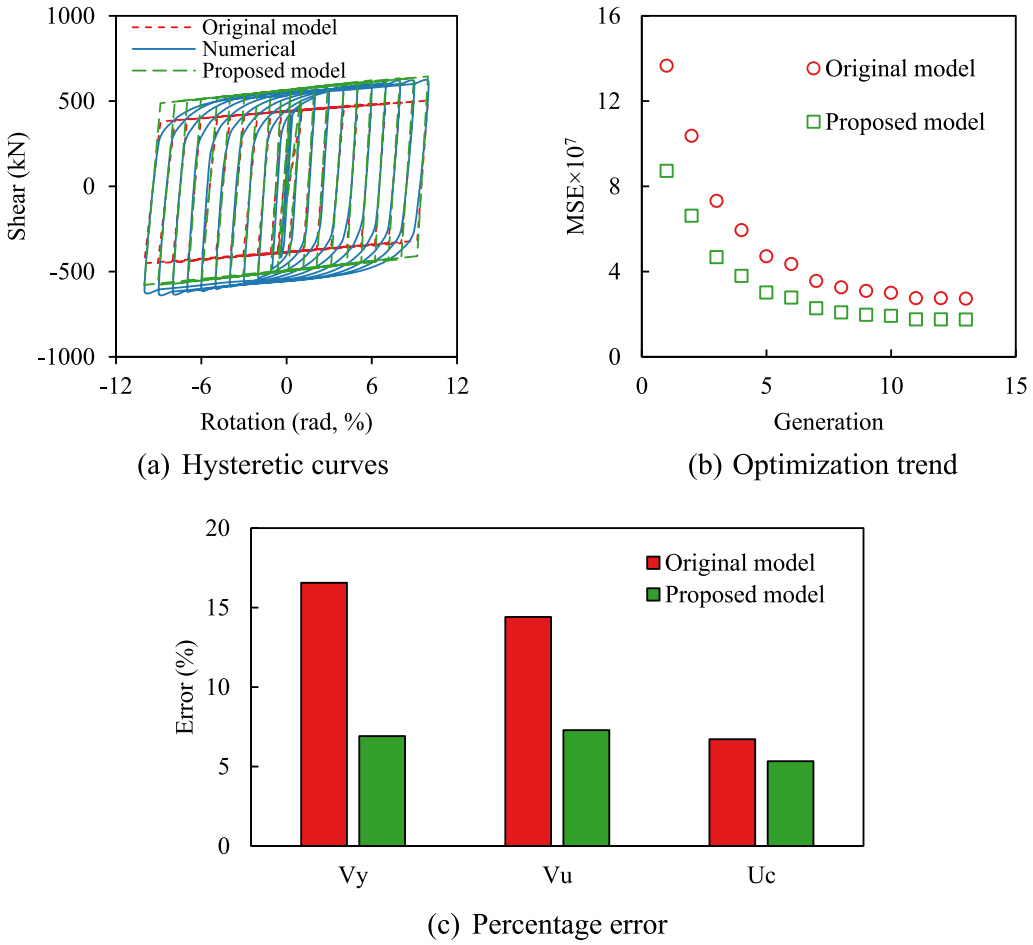

Fig. 23. Comparison between the numerical results and the analytical models.

stabilizes, while test MSE decreases until it hits the minimum value at 20 neurons before rising again. This trend suggests that 20 neurons is optimal, achieving the lowest test MSE and avoiding overfitting, as additional neurons only increase test MSE.

The inherent stochastic nature of ANN training means that each training session may yield different MSE and R^2 values. This variability arises from factors such as the random initialization of weights, shuffling of training data, and stochastic elements in gradient-based optimization algorithms.

Random initialization affects the starting conditions of the optimization, potentially leading the model to different local minima. Shuffling of data during each epoch results in varied mini-batch formations, influencing the optimization path. Additionally, the use of stochastic gradient descent or similar methods introduces randomness in gradient calculations, adding further variability to training outcomes.

To account for these factors and ensure optimal performance, the network was trained over 400 iterations. The model from the 93rd iteration, which achieved the lowest MSE of 0.0011 was selected as the final, optimized ANN model [72].

5.2.2. *Performance of the artificial neural network (ANN)*

After the training phase, assessing the ANN's performance is crucial to confirm its efficacy and reliability. Fig. 26 presents the relationship between the number of epochs and the MSE during both training and testing phases. As the number of epochs increases, the training MSE consistently decreases, demonstrating the model's progressive improvement in fitting the training data. In contrast, the test MSE follows a different trend; it initially decreases, reflecting enhanced generalization, but stabilizes after a certain point, suggesting that additional training does not further enhance performance on the test data.

The ANN achieved its best training performance at the 630th epoch, with the training MSE leveling off at approximately 1.6×10^{-5}. Beyond this point, while the training MSE continues to decline, the test MSE remains constant, signaling potential overfitting. Therefore, 630 epochs are deemed optimal for achieving the best test performance while mitigating overfitting.

The error histogram in Fig. 27 shows the distribution of prediction errors for both training and testing data. Most errors are clustered around zero, indicating high accuracy. The training errors are slightly more concentrated, suggesting better fit to the training data. While a few outliers exist, the overall performance demonstrates effective training and accurate predictions.

Fig. 28 shows a strong correlation between predicted and actual values, with data points closely aligned along the identity line. The high R^2 value of 0.9998 further confirms this excellent fit. These results indicate that the ANN effectively learned the data and achieved accurate predictions in both training and testing phases.

5.2.3. *Effect of input features on the outputs of the artificial neural network (ANN)*

To better understand the impact of different input parameters on the outputs of the ANN, the combined permutation importance plot in Fig. 29 can be utilized. Permutation importance involves shuffling the values of each feature and measuring the resulting change in model performance. This approach highlights the importance of each feature by quantifying the increase in prediction error when the feature's information is disrupted.

The plot demonstrates that features such as h_w/t_w and t_w significantly

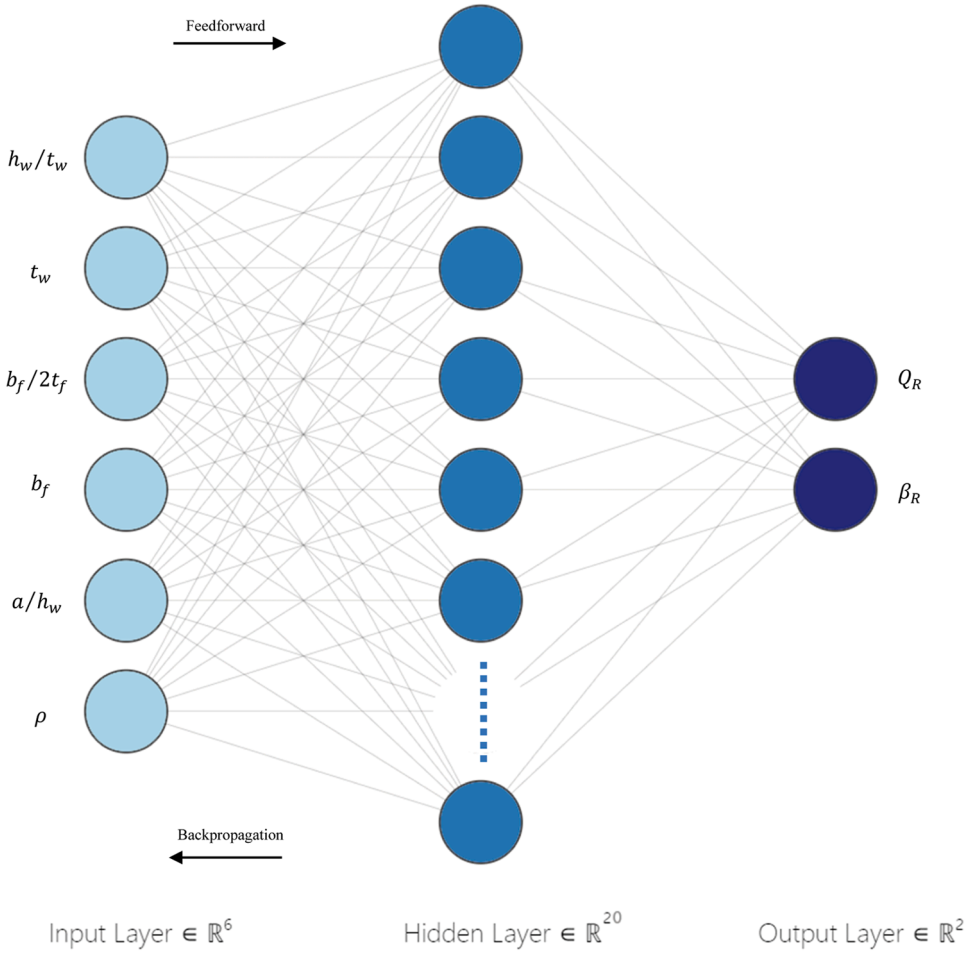

Fig. 24. Architecture of the incorporated ANN.

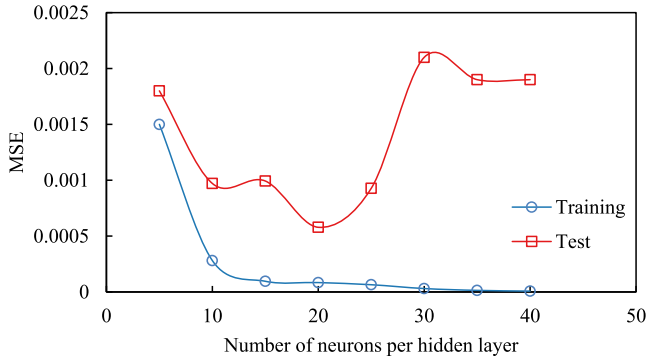

Fig. 25. Number of neurons in the hidden layer and the corresponding MSE.

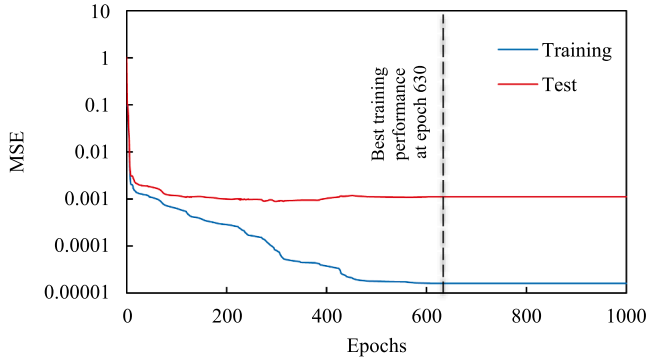

Fig. 26. Performance plot of the ANN.

influence model performance for both outputs. Specifically, h_w/t_w has an importance score of 0.90 for Q_R and 0.44 for β_R, while t_w has an importance score of 0.26 for Q_R and 0.59 for β_R. Conversely, features like $b_f/2t_f$, ρ, and b_f have negligible effects on both outputs, with importance scores close to zero, indicating that these parameters do not significantly impact the ANN's performance. These visualizations are crucial for pinpointing both influential and less influential features, thereby enhancing the interpretability and effectiveness of the model.

5.2.4. Derivation of predictive formulas from the artificial neural network (ANN)

Since the application of a trained ANN typically requires the user to have a copy of the trained model, this section addresses the need for deriving explicit formulas for the hardening parameters Q_R and β_R. These formulas enable the calculation of these parameters analytically, providing a practical solution for cases where the ANN itself is unavailable. By extracting and detailing the weight matrices and bias vectors from the trained ANN, a method to replicate the model's predictive capabilities through explicit equations is offered herein.

This approach facilitates the use of the model's predictions in analytical contexts, ensuring accessibility and usability without direct reliance on the ANN. It is crucial to emphasize that these formulas are applicable exclusively to shear link dampers that possess the geometric and material properties outlined in Table 5 and are made of Q345GJ steel, as the ANN

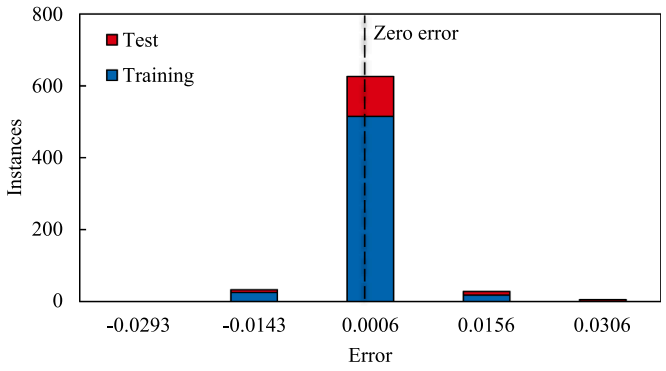

Fig. 27. Error histogram.

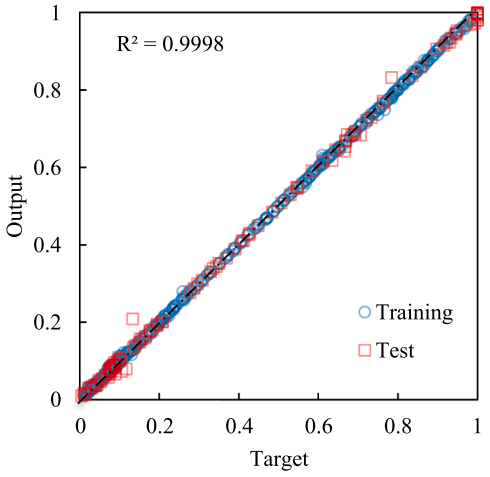

Fig. 28. Regression plot for the ANN.

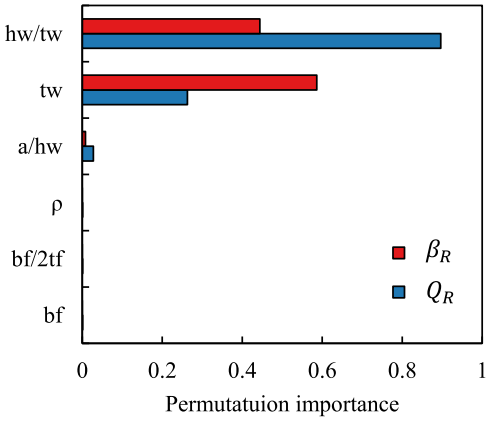

Fig. 29. Permutation importance plot.

was trained using data confined to these specific ranges.

As mentioned earlier, the ANN consists of an input layer with six nodes corresponding to the input parameters h_w/t_w, t_w, $b_f/2t_f$, b_f, a/h_w, and ρ. The network features a single hidden layer with 20 neurons and an output layer that includes two neurons, each representing the outputs Q_R and β_R.

Given that the numerical formulas are too complex to handle directly, the matrix forms are adopted for the calculations. To compute the hidden layer neuron outputs (H), the following transformation is applied:

$$H = \tanh\left(W_h{}^T X + b_h\right) \tag{27}$$

where X is the input vector, $W_h{}^T$ is the transpose of the weight matrix

Table 5
Values range for the input parameters.

Range	h_w/t_w	t_w (mm)	$b_f/2t_f$	b_f (mm)	a/h_w	ρ
Minimum	13.88	5	5	100	0.21	0.54
Maximum	50	18	7	140	1.05	1.59

W_h for the hidden layer, and b_h is the bias vector for the hidden layer. All these parameters can be obtained as follows:

$$X = \begin{bmatrix} h_w/t_w \\ t_w \\ b_f/2t_f \\ b_f \\ a/h_w \\ \rho \end{bmatrix} \tag{28}$$

$$W_h{}^T = \begin{bmatrix} W_{h1,1} & \cdots & W_{h1,6} \\ \vdots & \ddots & \vdots \\ W_{h20,1} & \cdots & W_{h20,6} \end{bmatrix} \tag{29}$$

$$b_h = \begin{bmatrix} b_{h1,1} \\ \vdots \\ b_{h20,1} \end{bmatrix} \tag{30}$$

where the elements of $W_h{}^T$ and b_h matrices are listed in Table 6.

Given that the final outputs Q_R and β_R are provided in the output vector Y, the latter can be obtained as follows:

$$Y = \begin{bmatrix} Q_R \\ \beta_R \end{bmatrix} = W_o{}^T H + b_o \tag{31}$$

where $W_o{}^T$ is the transpose of the weight matrix W_o for the output layer, and b_o is the bias vector for the output layer. All these parameters can be obtained as follows:

$$W_o{}^T = \begin{bmatrix} W_{o1,1} & \cdots & W_{o1,20} \\ W_{o2,1} & \cdots & W_{o2,20} \end{bmatrix} \tag{32}$$

$$b_o = \begin{bmatrix} 1.515 \\ -0.680 \end{bmatrix} \tag{33}$$

where the elements of $W_o{}^T$ matrix are listed in Table 7.

Consequently, substituting the specific properties of the shear link damper as inputs in Eqs. (27) to (33) yields the hardening parameters Q_R and β_R. These parameters can then be used to predict the hysteretic response of the damper in accordance with Eq. (24).

5.2.5. *Blind validation of the proposed analytical model*

Throughout this paper, new formulas have been derived to estimate the yield shear strength, cyclic web shear buckling rotation angle, and elastic stiffness of shear link dampers. Additionally, a novel hysteretic restoring force model has been developed. These approaches for shear link damper modeling have been calibrated against experimental results to ensure reliability, with blind validation presented in this section.

Blind validation refers to testing the model's predictive accuracy against datasets not utilized in the derivation of the analytical formulas or in the training phase of the ANN. For this purpose, nine out of ten shear link dampers tested experimentally by Liu et al. [50] and two out of three by Hu et al. [79] were included in the blind validation.

The properties of Liu et al.'s [50] specimens are shown in Table 1, while those of Hu et al.'s [79] specimens are presented in Table 8. For Liu et al.'s [50] specimens, the specimen labeled "RSL-1" was excluded from validation, as it lacked transverse stiffeners and thus differed significantly from the 350 specimens used to derive the analytical model and train the ANN. Similarly, the "SL-2" specimen from Hu et al.'s [79] experimental tests was excluded due to its one-sided stiffener

Table 6
Elements of $W_h{}^T$ and b_h matrices.

$W_h{}^T$							b_h
Row	Column						Column
	1	2	3	4	5	6	1
1	−1.976	−0.048	0.755	−0.048	−0.12	0.967	1.154
2	0.122	0.751	0.109	−0.194	0.436	−0.122	−1.577
3	−0.798	−0.63	−0.234	0.142	3.186	−0.135	2.062
4	−2.51	−1.236	0.268	−0.072	−2.744	0.388	−2.939
5	−2.249	1.683	0.577	0.529	−3.274	1.972	−0.635
6	−6.42	4.137	1.508	1.588	−0.774	4.258	5.748
7	−0.168	−1.664	0.072	−0.15	0.054	0.043	−0.413
8	2.556	−3.133	−0.753	−0.553	2.369	−1.765	−0.377
9	0.099	−0.204	−0.295	0.3	0.754	0.126	−0.784
10	0.073	0.468	−0.171	0.243	0.92	0.134	−0.311
11	−0.152	−0.063	−0.511	0.289	−0.146	−0.411	1.053
12	2.382	1.631	−0.038	−0.528	4.673	−1.383	4.412
13	−2.001	−0.358	0.37	0.304	−0.13	1.006	1.303
14	−2.562	1.918	0.287	0.777	−3.71	1.745	−0.299
15	−2.807	1.439	0.648	0.563	−0.307	1.573	2.365
16	−1.203	0.903	0.222	0.323	−0.089	0.596	1.427
17	−0.366	0.722	−0.221	0.099	2.531	−0.479	2.361
18	−3.415	2.132	0.596	0.778	−2.201	2.012	−0.07
19	−0.736	−0.098	0.018	0.164	−1.356	0.564	−1.025
20	−0.1	−1.07	0.025	0.049	−0.53	0.384	−0.111

Table 7
Elements of $W_o{}^T$ matrix.

Column	Row	
	1	2
1	1.340	0.997
2	1.407	0.011
3	−0.549	−0.759
4	−1.022	0.913
5	0.124	−0.571
6	−0.145	0.707
7	−0.258	−0.881
8	−0.503	1.936
9	−0.861	−0.225
10	0.181	1.002
11	−1.393	0.212
12	−0.440	0.974
13	−0.260	−0.862
14	−0.124	0.555
15	−0.014	−0.875
16	−1.279	0.660
17	0.724	0.990
18	−0.502	1.921
19	0.608	−0.139
20	−0.530	1.336

configuration, which did not align with the stiffening used in the reference dataset.

Using the geometric properties of the specimens, the yield shear strength, cyclic web shear buckling rotation angle, elastic stiffness, and hardening parameters were computed using the derived analytical model and the ANN. These values were then applied to generate hysteretic curves, which were subsequently compared with the experimental results provided by Liu et al. [50] and Hu et al. [79].

For instance, as illustrated in Fig. 30(a), for specimen RSL-2 of Liu et al. [50], the ANN-predicted curves exhibit a regular and smooth pattern that closely follows the experimental trend, albeit with reduced variability. This comparison indicates that while the ANN model effectively captures the general shape and key features of the hysteretic response, it may not fully replicate the detailed variability observed in experimental results. This discrepancy is partially due to the bilinear nature of the proposed analytical model, as discussed in detail in Section 4.

To further assess the model's accuracy, the ratio k between the cumulative dissipated energy from the ANN-predicted hysteretic curve and that from the experimental curve was calculated, yielding a value of 0.84. This suggests that, despite slight differences in curve matching, the ANN-predicted hysteretic curves exhibit energy-dissipative behavior comparable to that observed experimentally. This ratio underscores the ANN's capability to approximate the energy dissipation characteristics of the physical system, thus highlighting its potential in predictive modeling.

Fig. 30(b) provides a box plot of the ratios between the predicted yield shear strength (V_y), cyclic web buckling rotation angle (γ_b), elastic stiffness (K_e), and cumulative dissipated energy (U_c) and their experimental counterparts from the experimental tests of Liu et al. [50] and Hu et al. [79]. The boxes represent the middle 50 % of the data, with whiskers extending to the extreme data points within 1.5 times the interquartile range.

Overall, the predicted parameters closely align with the experimental values, with a median near 1.0, indicating no systematic over- or under-prediction. However, some variability is observed, with certain predicted parameters differing from experimental values. Whiskers indicate extreme values, ranging from a ratio of 1.22 to 0.84, demonstrating a range of variability. The predictions for V_y and γ_b show greater variability compared to K_e and U_c, where the predictions are more tightly clustered around the median.

Based on the blind validation conducted on two distinct groups of specimens from independent experimental studies, it can be concluded that the proposed analytical model accurately simulates the response of shear link dampers. The consistency observed across diverse datasets indicates that the model not only generalizes well to untested conditions but also provides a reliable framework for predictive modeling in practical applications.

Table 8
Properties of Hu et al.'s [50] specimens.

Specimen	h_w (mm)	t_w (mm)	b_f (mm)	t_f (mm)	a (mm)	t_s (mm)	e (mm)	ρ
SL−1	286	6	150	8	130	10	650	1.36
SL−3	286	6	150	8	220	10	650	1.36

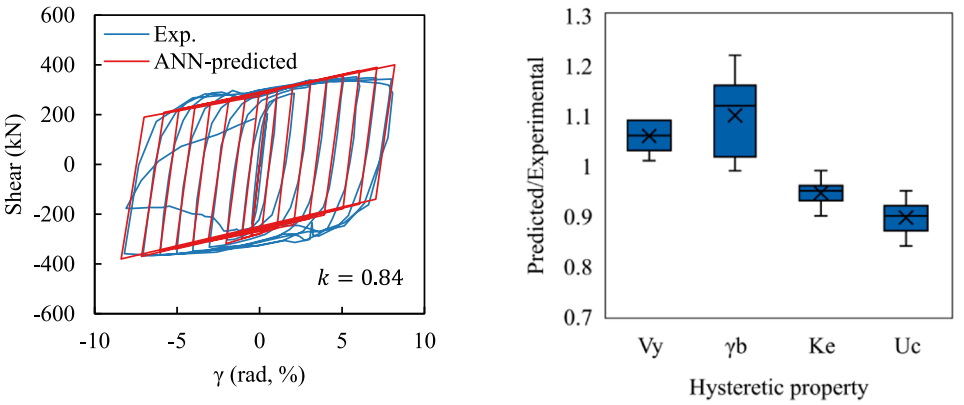

(a) Hysteretic curves for RSL-2 of Liu et al. [50]

(b) Boxplot with ratio of the predicted parameters to the experimental ones

Fig. 30. Comparison between ANN-predicted results and experimental results reported by Liu et al. [50] and Hu et al. [79].

5.2.6. Incorporation of the analytical model in a graphical user interface (GUI)

Since the developed analytical model's accuracy was confirmed, the model was incorporated into a component within the software entitled SL-Analyser, dedicated to the analytical modeling and analysis of shear links. This software is presently undergoing development by the authors. The graphical user interface (GUI) corresponding to this particular segment of the software is depicted in Fig. 31, and it is also provided as a supplementary material.

In the GUI, the user is required to define the values for eight inputs representing the geometric properties of the shear link damper, provided that they fall within the range previously specified in Table 5. Upon clicking the "Predict" button, the inputs are substituted ~~in~~ into the derived formulas and the trained ANN to estimate the values of the five outputs representing the bedrock of the proposed analytical model. To facilitate the practical implementation of the proposed analytical model, an illustrative example is provided in Appendix A.

6. Conclusions

In this study, 350 Q345GJ steel shear link dampers were numerically analyzed, considering various geometric properties alongside geometric imperfections and material nonlinearity. Additionally, an enhanced restoring force model was developed and optimized through a genetic algorithm to determine its optimal hardening parameters. To address the difficulties in predicting these parameters, an artificial neural network (ANN) was trained and blindly tested for evaluation. Key findings are summarized below.

(a) The numerical yield shear strength and the plastic shear capacity calculated as per ANSI/AISC 341-16 [6] showed minor deviations across all 350 specimens. Therefore, a new formula (Eq. 8) was proposed to correlate them. The proposed formula accounts for 99.98 % of the variability in the yield shear strength based on the plastic shear capacity.

(b) Among the investigated geometric parameters, only the web slenderness ratio and the link length ratio impact the plastic overstrength, with strong correlations indicated by absolute

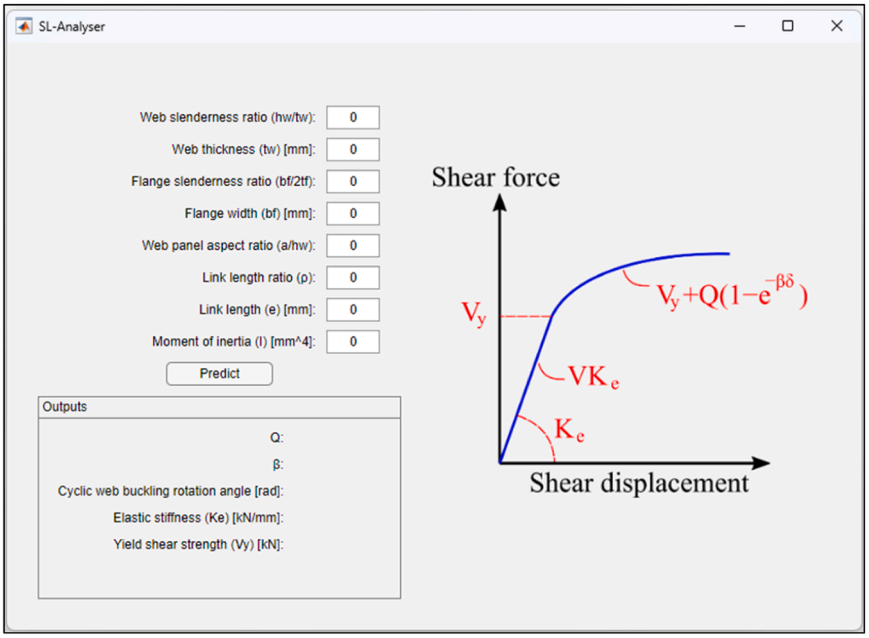

Fig. 31. GUI of SL-Analyser.

Pearson correlation coefficients of 0.91 and 0.89, respectively. Conversely, the flange slenderness ratio and web panel aspect ratio exhibited minimal influence, resulting in substantially lower absolute Pearson correlation coefficients of 0.24 and 0.27, respectively.

(c) The one-variable-at-a-time (OVAT) analysis highlighted the substantial impact of the web slenderness ratio and web panel aspect ratio on the cyclic web shear buckling rotation angle, unlike the flange slenderness ratio. So, Eq. (11) was derived to predict the cyclic web shear buckling rotation angle, considering these influential parameters. With a coefficient of determination of 0.995, the formula exhibits an exceptionally high level of goodness of fit.

(d) The study highlights that the current analytical methods based on FEMA 356 for estimating the elastic stiffness of shear link dampers tend to underestimate the actual values. A proposed modification using the power law presented in Eq. (15) demonstrates a high accuracy, accompanied by a coefficient of determination of 0.998, indicating that this refined formula provides more precise and reliable predictions for the elastic stiffness of shear link dampers.

(e) The proposed restoring force model demonstrated superior fidelity to hysteretic curves compared to the original model. Following the optimization process, the proposed model exhibited a lower mean squared error than the original one. Moreover, it predicted yield shear strength, peak shear strength, and cumulative dissipated energy with an average error of around 6 %, whereas the original model had an average error of approximately 13 %. This twofold reduction in error highlights the effectiveness of the proposed model in simulating the hysteretic response of shear link dampers.

(f) The developed ANN exhibited a low error rate and avoided bias toward overestimation or underestimation of target values. It consistently generated predictions with few outliers and achieved a superior coefficient of determination of 0.9998, indicating effective handling of most data points. This performance underscores a well-trained ANN capable of generalizing effectively to new data.

(g) The blind validation confirmed the ability of the proposed analytical model to predict hysteretic parameters and curves matching experimental tests. Additionally, the ratio between yield shear strength, cyclic web buckling rotation angle, elastic stiffness, and cumulative energy dissipation obtained from the analytical model and experimental results averaged at 0.99, reinforcing confidence in the analytical model's reliability.

While the proposed model provides a reliable simulation of the shear link damper's behavior, certain limitations remain that could be addressed in future research. An important limitation of the current model is its inability to predict the ultimate load-carrying capacity or the definite point beyond which strength deterioration occurs in shear link dampers. This issue is addressed in part by terminating the response at the cyclic web shear buckling rotation angle; however, further research could focus on refining the model to predict post-buckling behavior and ultimate failure. Investigating curvilinear models or alternative termination criteria may provide insights into more accurately simulating the full range of the damper's behavior, representing a valuable direction for future study.

CRediT authorship contribution statement

Ahmed Elgammal: Writing – review & editing, Writing – original draft, Visualization, Validation, Software, Resources, Methodology, Formal analysis, Data curation, Conceptualization, Investigation. **Yasmin Ali:** Conceptualization, Data curation, Software, Validation, Visualization, Writing – review & editing.

Declaration of Competing Interest

The authors declare that they have no known competing financial interests or personal relationships that could have appeared to influence the work reported in this paper.

Appendix A. . Implementation guide for the analytical model of shear link dampers

This appendix outlines the step-by-step process required to implement the proposed analytical model for predicting the hysteretic response of shear link dampers. Additionally, it demonstrates how to incorporate the predicted response into software commonly used for general analysis of structures equipped with these specific dampers.

The accompanying flowchart in Fig. A1 visualizes the process, illustrating each phase from initial input of damper properties to final integration with external software. This flowchart and step-by-step explanation together provide a procedural algorithm, detailing the progressive steps required to implement the proposed model accurately.

To utilize the proposed analytical model effectively, five distinct phases are required, as illustrated in Fig. A1. These phases are explained in detail, beginning with the input and verification of damper properties and culminating in the generation of the force-displacement curve for integration into relevant analysis software.

- **Phase 1:** The user begins by inputting key geometric properties of the shear link damper, including web height, web thickness, flange width, flange thickness, stiffener spacing, and length. These inputs are used to calculate dimensional ratios such as web slenderness ratio, flange slenderness ratio, web panel aspect ratio, and length ratio, ensuring that the damper's properties fall within the calibrated ranges listed in Table 4. If any values fall outside these ranges, a caution is noted that the model's predictions may be less accurate.
- **Phase 2:** Based on the damper properties, the hardening parameters Q_R and β_R should be calculated. This can be achieved either by manually substituting values into Eqs. (27)–(33) or by using the provided GUI software, which automates the calculations through an ANN-trained approach. The GUI option is recommended for ease and accuracy.
- **Phase 3:** Next, the user calculates the damper's elastic stiffness using Eqs. (12)–(15) or using the GUI software. The same applies to the yield shear strength, which can be either estimated using Eqs. (7) and (8) or using the GUI software. Once the elastic stiffness and yield shear strength are obtained, the yield displacement is determined by dividing the yield shear strength by the elastic stiffness.
- **Phase 4:** With the parameters now defined, the load-displacement curve can be generated in two stages—covering the elastic phase and the kinematic hardening phase. This curve is constructed using Eq. (24). The curve is terminated when the damper reaches its cyclic web shear buckling rotation angle, which is calculated using Eq. (11). Beyond this rotation angle, the damper's response begins to deteriorate, so the displacement corresponding to this angle marks the endpoint of the foce-displacement curve.

- **Phase 5:** The final force-displacement curve represents the skeleton or backbone curve for the damper. This curve can now be exported and incorporated into general-purpose analysis software to model the behavior of the shear link damper within broader structural systems.

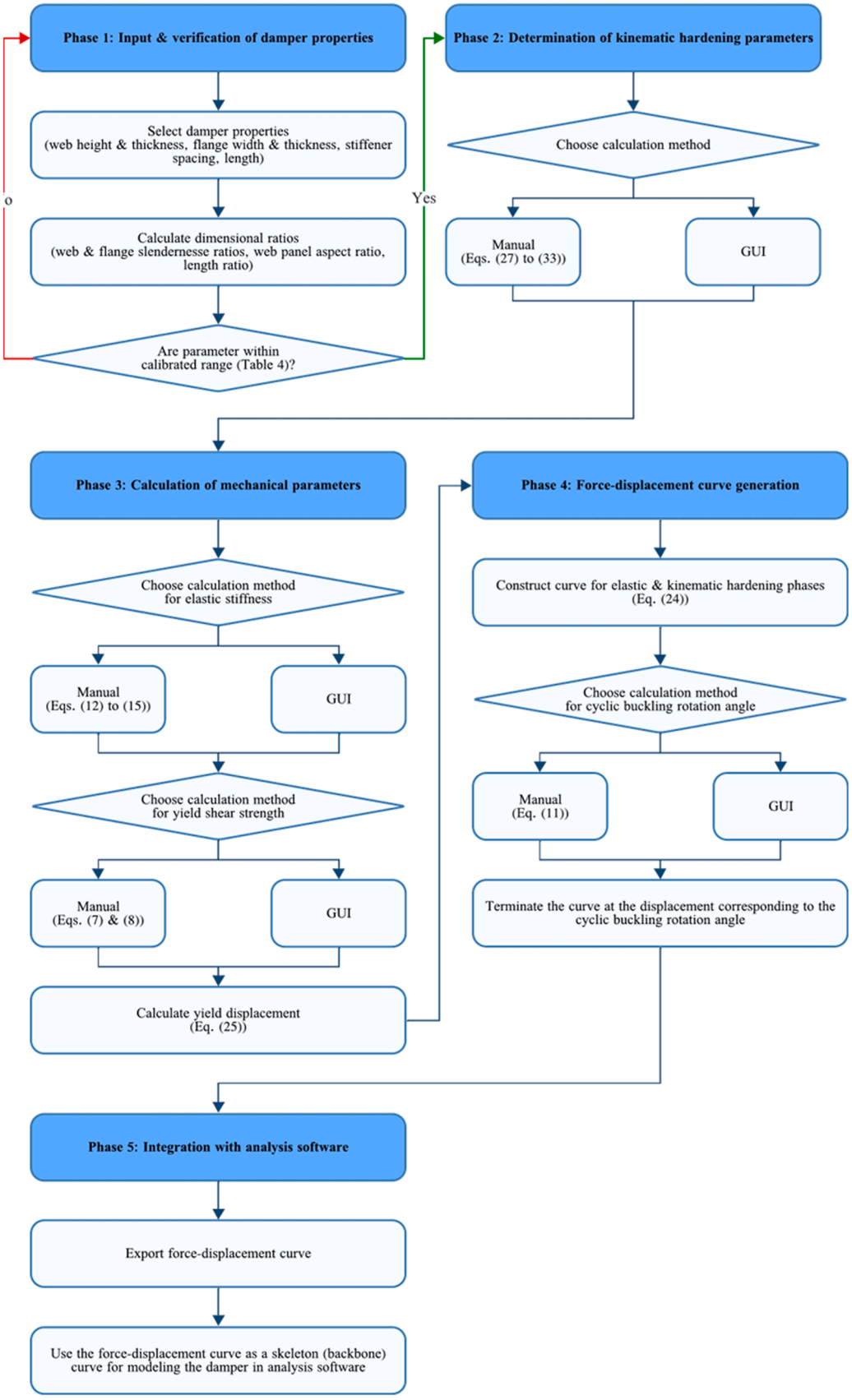

Fig. A1. Flowchart for implementing the proposed analytical model for predicting the hysteretic response of shear link dampers.

.

Appendix B. Supporting information

Supplementary data associated with this article can be found in the online version at doi:10.1016/j.istruc.2024.107848.

References

[1] Elgammal A. Improving the Performance of Vertical Shear Links for Enhanced Seismic Energy Dissipation. MSc thesis, Tanta University; 2021.
[2] Saaed T.E., Nikolakopoulos G., Jonasson J.-E., Hedlund H. A state-of-the-art review of structural control systems. https://doi.org/10.1177/1077546313478294.
[3] Castaldo P. Integrated Seismic Design of Structure and Control Systems. Cham: Springer International Publishing; 2014.
[4] Ranjan Sahoo D., Singhal T., Singh Taraithia S., Saini A. (2015) Cyclic behavior of shear-and-flexural yielding metallic dampers. JCSR 114:247–257. https://doi.org/10.1016/j.jcsr.2015.08.006.
[5] Popov EP, Engelhardt MD. Seismic eccentrically braced frames. J Constr Steel Res 1988;10:321–54.
[6] American Institute of Steel Construction (AISC) (2016) Seismic provisions for structural steel buildings: ANSI/AISC 341–16. Chicago, Illinois, USA.
[7] Hjelmstad KD, Popov EP. Seismic Behavior of Active Beam Links in Eccentrically Braced Frames. University of California; 1983.
[8] Hjelmstad KD, Popov EP. Cyclic behavior and design of link beams. J Struct Eng 1983;109:2387–403. https://doi.org/10.1061/(ASCE)0733-9445(1983)109:10(2387).
[9] Kasai K, Popov EP. General behavior of WF steel shear link beams. J Struct Eng 1986;112:362–82. https://doi.org/10.1061/(ASCE)0733-9445(1986)112:2(362).
[10] Richards PW. Cyclic stability and capacity design of steel eccentrically braced frames. University Of California,; 2004.
[11] Chao S-H, Khandelwal K, El-Tawil S. Ductile web fracture initiation in steel shear links. J Struct Eng 2006;132:1192–200. https://doi.org/10.1061/(asce)0733-9445(2006)132:8(1192).
[12] Ghadami A., Pourmoosavi G., Talatahari S., Farahmand Azar B. (2021) Overstrength factor of short low-yield-point steel shear links. https://doi.org/10.1016/j.tws.2021.107473.
[13] El-Khoriby S., Seleemah A., Elgammal A. (2020) Cyclic performance of vertical shear links made of different metallic alloys. International Journal of Advances in Structural and Geotechnical Engineering 4:1–14. https://doi.org/10.21608/asge.2020.271201.
[14] Yurisman, Budiono B, Moestopo M, Suarjana M. Behavior of shear link of WF section with diagonal web stiffener of eccentrically braced frame (EBF) of steel structure. ITB J Eng Sci 2010;42 B:103–28. https://doi.org/10.5614/itbj.eng.sci.2010.42.2.1.
[15] Ghamari A, Alzeebaree R, Thongchom C. Developing an innovative stiffened shear damper for concentrically braced frames. Structures 2023;50:734–44. https://doi.org/10.1016/J.ISTRUC.2023.02.079.
[16] Nuzzo I, Losanno D, Caterino N, et al. Experimental and analytical characterization of steel shear links for seismic energy dissipation. Eng Struct 2018;172:405–18. https://doi.org/10.1016/j.engstruct.2018.06.005.
[17] Elgammal A, Hassanein MF, Seleemah A. Enhancing the cyclic performance of shear links using longitudinal stiffeners. J Constr Steel Res 2023;211:108200. https://doi.org/10.1016/j.jcsr.2023.108200.
[18] Ghadami A, Pourmoosavi G, Ghamari A. Seismic design of elements outside of the short low-yield-point steel shear links. J Constr Steel Res 2021;178. https://doi.org/10.1016/J.JCSR.2020.106489.
[19] He J, Feng S, Teng Q, et al. Hysteretic behavior of replaceable low yield point steel links with corrugated web. Thin-Walled Struct 2024;194:111330. https://doi.org/10.1016/j.tws.2023.111330.
[20] Sabouri-Ghomi S., on MZ-T 14th WC, 2008 undefined A study on the behavior of shear link beam made of easy-going steel in eccentrically braced frames. 1284615421.
[21] Chacón R, Vega A, Mirambell E. Numerical study on stainless steel I-shaped links on eccentrically braced frames. J Constr Steel Res 2019;159:67–80. https://doi.org/10.1016/j.jcsr.2019.04.014.
[22] El-Khoriby S, Seleemah A, El-Gammal A. Cyclic performance of vertical shear links made of different metallic alloys. Proc Int Conf Adv Struct Geotech Eng (ICASGE'19) Hurghada, Egypt 2019.
[23] Seleemah A, El-Khoriby S, El-Gammal A. Seismic response of 2-D plane framed buildings eccentrically braced with vertical shear links. Int J Adv Struct Geotech Eng 5 2021:1–18. https://doi.org/10.21608/ASGE.2022.152698.1006.
[24] El-Khoriby S, Seleemah A, El-Gammal A. Seismic response of 2-D framed buildings eccentrically braced with vertical shear links. : Proc Int Conf Adv Struct Geotech Eng Hurghada 2021.
[25] Rides JM, Popov EP. Inelastic link element for EBF seismic analysis. J Struct Eng 1994;120:441–63. https://doi.org/10.1061/(ASCE)0733-9445(1994)120:2(441).
[26] Ramadan T, Ghobarah A. Analytical model for shear-link behavior. J Struct Eng 1995;121:1574–80. https://doi.org/10.1061/(ASCE)0733-9445(1995)121:11(1574).
[27] Richards P., Uang C.-M. (2003) Development of testing protocol for short links in eccentrically braced frames: (Report No. SSRP–2003/08). San Diego, CA.
[28] Zhuang L, Wang J, Nie X, Wu Z. Experimental study on the cyclic behaviour of shear links made of BLY160 steel. Thin-Walled Struct 2022;174. https://doi.org/10.1016/j.tws.2022.109072.
[29] Xu L-Y, Nie X, Fan J-S. Cyclic behaviour of low-yield-point steel shear panel dampers. Eng Struct 2016;126:391–404. https://doi.org/10.1016/j.engstruct.2016.08.002.
[30] Vaiana N, Rosati L. Classification and unified phenomenological modeling of complex uniaxial rate-independent hysteretic responses. Mech Syst Signal Process 2023;182:109539. https://doi.org/10.1016/j.ymssp.2022.109539.
[31] Vaiana N, Rosati L. Analytical and differential reformulations of the Vaiana–Rosati model for complex rate-independent mechanical hysteresis phenomena. Mech Syst Signal Process 2023;199:110448. https://doi.org/10.1016/j.ymssp.2023.110448.
[32] Thai H-T. Machine learning for structural engineering: a state-of-the-art review. Structures 2022;38:448–91. https://doi.org/10.1016/j.istruc.2022.02.003.
[33] Slowik A., Kwasnicka H. (2020) Evolutionary algorithms and their applications to engineering problems. Neural Comput Appl 32:12363–12379. https://doi.org/10.1007/S00521–020-04832–8/TABLES/4.
[34] Razavi SA, Siahpolo N, Mahdavi Adeli M. A new empirical correlation for estimation of EBF steel frame behavior factor under near-fault earthquakes using the genetic algorithm. J Eng 2020;2020:1–13. https://doi.org/10.1155/2020/3684678.
[35] Rumelhart DE, Hinton GE, Williams RJ. Learning representations by back-propagating errors. Nature 1986;323:533–6. https://doi.org/10.1038/323533a0.
[36] Sun H, Burton HV, Huang H. Machine learning applications for building structural design and performance assessment: state-of-the-art review. J Build Eng 2021;33:101816. https://doi.org/10.1016/j.jobe.2020.101816.
[37] Bae J., Jang A., Park M.J., et al. (2022) Steel and Composite Structures. Steel and Composite Structures 43:501. https://doi.org/10.12989/SCS.2022.43.4.501.
[38] Bae J, Lee C-H, Park M, et al. Modified low-cycle fatigue estimation using machine learning for radius-cut coke-shaped metallic damper subjected to cyclic loading. Int J Steel Struct 2020;20:1849–58. https://doi.org/10.1007/s13296-020-00377-7.
[39] Chalabi R, Yazdanpanah O, Dolatshahi KM. Nonmodel rapid seismic assessment of eccentrically braced frames incorporating masonry infills using machine learning techniques. J Build Eng 2023;79:107784. https://doi.org/10.1016/j.jobe.2023.107784.
[40] Ansys Inc. (2023) Ansys Workbench (2023 R1)
[41] MathWorks Inc (2023) MATLAB R2023a (version: 9.14)
[42] Lee H-H. Finite Element Simulations with ANSYS Workbench 23: Theory, Applications, Case Studies. City of Mission: SDC Publications; 2023.
[43] Liu XG, Fan JS, Liu YF, et al. Theoretical research into cyclic web buckling and plastic overstrength of shear links. Thin-Walled Struct 2020;152:106644. https://doi.org/10.1016/j.tws.2020.106644.
[44] Miao F, Nejati F, Zubair SAM, Yassin ME. Seismic performance of eccentrical braced frame retrofitted by box damper in vertical links. Buildings 2022;12:1506. https://doi.org/10.3390/buildings12101506.
[45] Ghadami A, Broujerdian V. Shear behavior of steel plate girders considering variations in geometrical properties. J Constr Steel Res 2019;153:567–77. https://doi.org/10.1016/J.JCSR.2018.11.009.
[46] Okereke M., Keates S. (2018) Finite Element Mesh Generation. pp 165–186.
[47] Galić M, Draganić H, Dokšanović T. Finite Element Mesh Size Optimization for Steel Bolted Connection. In: EngOpt 2018 Proceedings of the 6th International Conference on Engineering Optimization. Cham: Springer International Publishing; 2019. p. 53–60.
[48] Goyal CR. Uncertainty Quantification in Non-linear Seismic Wave Propagation. M. Sc. thesis. Carleton University; 2017.
[49] Chaboche JL. Time-independent constitutive theories for cyclic plasticity. Int J Plast 1986;2:149–88. https://doi.org/10.1016/0749-6419(86)90010-0.
[50] Liu XG, Fan JS, Liu YF, et al. Experimental research of replaceable Q345GJ steel shear links considering cyclic buckling and plastic overstrength. J Constr Steel Res 2017;134:160–79. https://doi.org/10.1016/j.jcsr.2017.03.018.
[51] Pesaran Behbahani D, Fanaie N. Elimination of intermediate stiffeners in box link beam using low yield point steel. J Constr Steel Res 2022;188:107014. https://doi.org/10.1016/J.JCSR.2021.107014.
[52] Deng K, Pan P, Li W, Xue Y. Development of a buckling restrained shear panel damper. J Constr Steel Res 2015;106:311–21. https://doi.org/10.1016/j.jcsr.2015.01.004.
[53] EN 1993–1-5 (2007) Eurocode 3: Design of steel structures - Part 1–5: plated structural elements. European standard, Comité Européen de Normalisation, Brussels.
[54] Della Corte G, D'Aniello M, Landolfo R. Analytical and numerical study of plastic overstrength of shear links. J Constr Steel Res 2013;82:19–32.
[55] Özkilic YO. Optimized stiffener detailing for shear links in eccentrically braced frames. Steel Compos Struct 2021;39:35–50.
[56] Liu XG, Fan JS, Liu YF, et al. Theoretical research into cyclic web buckling and plastic overstrength of shear links. Thin-Walled Struct 2020;152. https://doi.org/10.1016/j.tws.2020.106644.
[57] Yadav D, Sahoo DR. Validation of hysteretic behavior and prediction of energy dissipation potential of aluminium shear yielding devices. Int J Mech Sci 2021;194:106204. https://doi.org/10.1016/j.ijmecsci.2020.106204.
[58] Kazemzadeh Azad S, Topkaya C. A review of research on steel eccentrically braced frames. J Constr Steel Res 2017;128:53–73. https://doi.org/10.1016/j.jcsr.2016.07.032.

[59] Ghamari A, Kim Y-J, Bae J. Utilizing an I-shaped shear link as a damper to improve the behaviour of a concentrically braced frame. J Constr Steel Res 2021;186:106915.
[60] Sim H-B, Fang Xiao-J, Uang C-M. Overstrength of I-Shaped Shear Links for EBF Design. Eng J 2023;60:21–30. https://doi.org/10.62913/engj.v60i1.1199.
[61] Zhu Y, Wang W, Lu Y, Yao Z. Finite element modeling and design recommendations for low-yield-point steel shear panel dampers. J Build Eng 2023;72:106634. https://doi.org/10.1016/j.jobe.2023.106634.
[62] Pourreza F, Mousazadeh M, Basim MCh. An efficient method for incorporating modeling uncertainties into collapse fragility of steel structures. Struct Saf 2021;88:102009. https://doi.org/10.1016/j.strusafe.2020.102009.
[63] Masoomzadeh M, Charkhtab Basim M, Chenaghlou MR, Khajehsaeid H. Probabilistic performance assessment of eccentric braced frames using artificial neural networks combined with correlation latin hypercube sampling. Structures 2023;48:226–40. https://doi.org/10.1016/j.istruc.2022.11.132.
[64] Federal Emergency Management Agency (FEMA) (2000) Prestandard and commentary for the Seismic rehabilitation of buildings (FEMA 356). Washington, D.C., USA
[65] Chaboche J., Van K., Cordier G. (1979) Modelization of the strain memory effect on the cyclic hardening of 316 stainless steel. Structural Mechanics in Reactor Technology, Berlin.
[66] Liu XG, Liu YF. Cyclic behavior of Q345GJ steel used in energy dissipation shear links. Int J Steel Struct 2016;16:697–704. https://doi.org/10.1007/s13296-015-0205-y.
[67] Vaiana N, Sessa S, Rosati L. A generalized class of uniaxial rate-independent models for simulating asymmetric mechanical hysteresis phenomena. Mech Syst Signal Process 2021;146:106984. https://doi.org/10.1016/j.ymssp.2020.106984.
[68] Vaiana N, Sessa S, Marmo F, Rosati L. A class of uniaxial phenomenological models for simulating hysteretic phenomena in rate-independent mechanical systems and materials. Nonlinear Dyn 2018;93:1647–69. https://doi.org/10.1007/s11071-018-4282-2.
[69] Goldberg D. (1989) Genetic Algorithms in Search, Optimization and Machine Learning. Addison-Wesley Professional, Boston.
[70] Moammer O, Dolatshahi KM. Predictive equations for shear link modeling toward collapse. Eng Struct 2017;151:599–612. https://doi.org/10.1016/j.engstruct.2017.08.052.
[71] Thai H-T. Machine learning for structural engineering: A state-of-the-art review. Structures 2022;38:448–91. https://doi.org/10.1016/j.istruc.2022.02.003.
[72] Zarringol M, Patel VI, Liang QQ, et al. Machine-learning-based predictive models for concrete-filled double skin tubular columns. Eng Struct 2024;304:117593. https://doi.org/10.1016/j.engstruct.2024.117593.
[73] Morfidis K, Kostinakis K. Approaches to the rapid seismic damage prediction of r/c buildings using artificial neural networks. Eng Struct 2018;165:120–41. https://doi.org/10.1016/j.engstruct.2018.03.028.
[74] MacKay DJC. Bayesian interpolation. Neural Comput 1992;4:415–47. https://doi.org/10.1162/neco.1992.4.3.415.
[75] Burden F., Winkler D. (2008) Bayesian Regularization of Neural Networks. pp 23–42.
[76] Rajabi E, Golestani Y. Study of steel buildings with LCF system under critical mainshock-aftershock sequence: Evaluation of fragility curves and estimation of the response modification factor by artificial intelligence. Structures 2023;56:105044. https://doi.org/10.1016/j.istruc.2023.105044.
[77] Yavuz Bayraktar O, Salem Taher Eshtewı S, Benli A, et al. The impact of RCA and fly ash on the mechanical and durability properties of polypropylene fibre-reinforced concrete exposed to freeze-thaw cycles and MgSO4 with ANN modeling. Constr Build Mater 2021;313:125508. https://doi.org/10.1016/j.conbuildmat.2021.125508.
[78] Cybenko G. Approximation by superpositions of a sigmoidal function. Math Control, Signals, Syst 1989;2:303–14. https://doi.org/10.1007/BF02551274.
[79] Hu S, Liu S, Zeng S, Shao T. Mechanical properties and influence factors of ordinary shear links. Buildings 2024;14:160. https://doi.org/10.3390/buildings14010160.